CrossMark

Textural and geochemical characteristics of late Pleistocene to Holocene fine-grained deep-sea sediment cores (GM6 and GM7), recovered from southwestern Gulf of Mexico

Abigail Anaya-Gregorio[1], John S. Armstrong-Altrin[2*], María Luisa Machain-Castillo[2], Patricia C. Montiel-García[3] and Mayla A. Ramos-Vázquez[4]

Abstract

Texture, mineralogy, geochemistry, and ^{14}C ages of two deep-sea sediment cores (GM6 and GM7) recovered in the southwestern Gulf of Mexico were investigated to infer their provenance and depositional condition. The sediments are enriched in fine-grained silt and clay and poor in sand content. Mineralogically, the sediments consist of quartz, calcite, smectite, and kaolinite. Based on the ^{14}C data, the age of the GM6 and GM7 sediment cores were calculated as 23,615 cal yrs. BP and 19,007 cal yrs. BP, respectively. The weathering indices such as chemical index of alteration (CIA), chemical index of weathering (CIW), and plagioclase index of alteration (PIA) in GM6 (56–69, 60–74, and 61–73, respectively) and GM7 (54–69, 57–76, and 55–74, respectively) cores revealed a moderate-to-high intensity of weathering. The rare earth element (REE) patterns suggested that the sediments were derived mostly by the weathering of intermediate rocks, exposed along the coastal regions of the Gulf of Mexico. The trace elemental ratios like V/Cr (<2), Ni/Co (<2), and Cu/Zn (<1), authigenic uranium content (<1), and Ce anomaly (Ce/Ce[*] ≤ 1) suggested that the sediments were deposited under an oxic condition, which was also revealed by the benthic foraminiferal assemblages throughout the GM6 and GM7 sediment cores.

Keywords: Radiocarbon age, Manganosite, Weathering, Palaeoredox condition, Provenance, Holocene, Gulf of Mexico

1 Introduction

The composition of terrigenous sediments is largely influenced by the nature of parent rocks and sedimentary processes during transportation and within the depositional basin (Armstrong-Altrin 2015; Basu 2017). Hence, the spatial and temporal variations during sedimentation can be able to understand by the mineralogical and geochemical compositions of sediments, and numerous studies utilized these as a device to understand sediment provenance (Bhattacharjee et al. 2017; Craigie 2018; Hou et al. 2017; Mitra et al. 2017; Paikaray et al. 2008; Saha et al. 2010,

2018; Verma et al. 2016a; Verma and Armstrong-Altrin 2016; Wang et al. 2017a, 2017b). In sediments, unstable minerals and mobile elements can be affected easily by weathering and erosional processes during transportation. However, immobile elements like REE, Co, Cr, Th, and Sc in sediments are considered as good provenance indicators, because they are not fractionated during sedimentary processes like diagenesis and weathering (Fedo et al. 1995). The fine-grained detrital sediments are particularly helpful for provenance study, because, they provide new insights into the sedimentation processes through geological time (Ramos-Vázquez et al. 2017; Selvaraj et al. 2015).

Previous studies by Carranza-Edwards et al. (2001) reported the composition of coastal sediments from the northwestern part of the Gulf of Mexico and inferred their provenance. Recently, Armstrong-Altrin et al. (2015a) and

* Correspondence: armstrong@cmarl.unam.mx; john_arms@yahoo.com
[2]Instituto de Ciencias del Mar y Limnología, Universidad Nacional Autónoma de México, Unidad de Procesos Oceánicos y Costeros, Ciudad Universitaria, 04510 Ciudad de México, Mexico
Full list of author information is available at the end of the article

Anaya-Gregorio et al. Journal of Palaeogeography (2018) 7:3

Page 2 of 19

Hernández-Hinojosa et al. (2018) investigated the origin of coastal sediments in the Veracruz and Tabasco states, Gulf of Mexico. Other studies documented the textural characteristics (Kasper-Zubillaga et al. 2013), heavy metal concentrations and geochemistry of estuary (Rosales-Hoz et al. 2015) and continental slope sediments (Armstrong-Altrin et al. 2015b; Ramos-Vázquez et al. 2017) from the western part of the Gulf of Mexico. Although numerous researchers investigated the provenance of coastal sediments along the Gulf of Mexico, studies concentrated on the textural and geochemical characteristics of fine-grained sediments in the southwestern Gulf of Mexico are little. In the present study,

we document texture, mineralogy, geochemistry, and ^{14}C age data of two fine-grained sediment cores (GM6 and GM7) retrieved in the southwestern Gulf of Mexico. The aims of this investigation are to investigate the chemical weathering, source rock composition, radiocarbon age, and the depositional condition.

2 Study area

Sampling of two sediment cores GM6 (Latitude 19°08′64.54″N and Longitude 93°59′81.90″W) and GM7 (Latitude 19°12′37.45″N and Longitude 94°06′13.15″W) (Fig. 1) was performed in the southwestern part of the

Fig. 1 Map showing core locations and geology of the Gulf of Mexico coastal areas (Source: Carta Geológica; scale 1:1,000,000) (modified after Armstrong-Altrin 2015). MVB = Mexican Volcanic Belt; EMAP = Eastern Mexican Alkaline Province

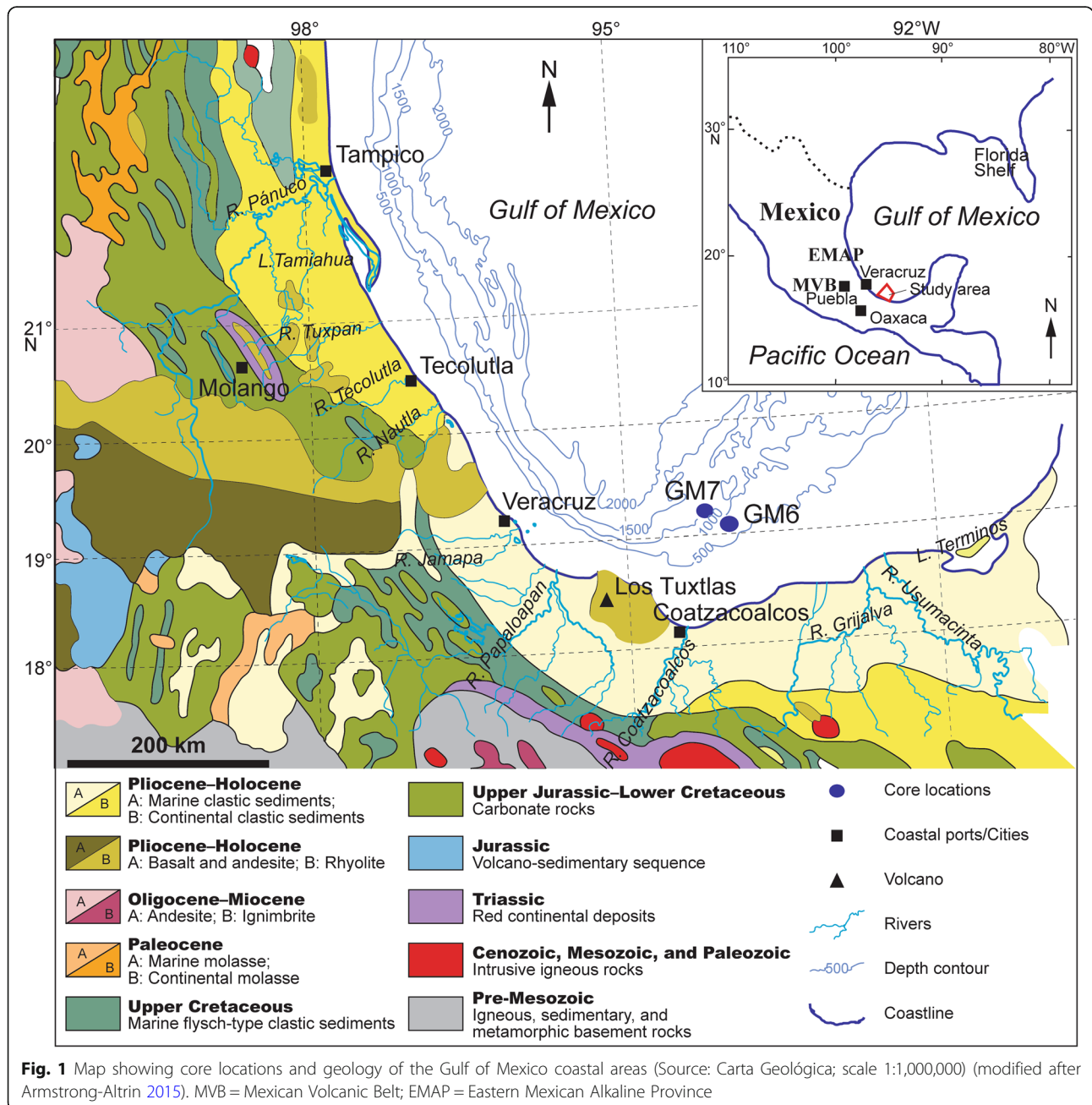Anaya-Gregorio et al. Journal of Palaeogeography (2018) 7:3

Page 3 of 19

Table 1 Grain size and textural parameters (Folk 1980) for the deep-sea sediments of the southwestern Gulf of Mexico

Core No.	GM6						GM7					
Water depth	856 m						989 m					
Latitude	19°08′64.54″N						19°12′37.45″N					
Longitude	93°59′81.90″W						94°06′13.15″W					
Section (cm)	0–1	91–92	151–152	222–223	300–301	Mean ± 1 s (n = 5)	0–1	91–92	151–152	222–223	300–301	Mean ± 1 s (n = 5)
Sand (%)	0.02	0.11	–	0.089	0.008	0.04 ± 0.05	–	–	–	0.299	0.003	0.06 ± 0.13
Silt (%)	52.3	50.9	48.2	49.4	51.5	50.5 ± 1.67	49.9	46.3	49.4	54.4	48.6	49.7 ± 2.93
Clay (%)	47.7	48.9	51.9	50.5	48.5	49.5 ± 1.67	50.2	53.7	50.7	45.4	51.4	50.3 ± 3.05
Mz (φ)	7.99	8.02	8.13	8.06	7.99	8.04 ± 0.06	8.07	8.17	7.99	7.80	8.07	8.02 ± 0.14
Sorting (σ1φ)	1.56	1.59	1.53	1.60	1.58	1.57 ± 0.03	1.54	1.57	1.73	1.74	1.65	1.64 ± 0.09
Skewness (Sk₁)	0.05	0.02	0.02	0.00	0.02	0.02 ± 0.01	0.03	0.02	0.07	0.02	0.03	0.03 ± 0.02
Kurtosis (K_G)	0.93	0.94	0.92	0.94	0.92	0.93 ± 0.01	0.93	0.95	0.93	0.94	0.93	0.94 ± 0.01

Gulf of Mexico, during a cruise program by a research vessel "Justo Sierra".

3 Geological backgrounds

A brief description about the rivers traversing along the southwestern Mexico and the geological setting of the study area is given below:

The Usumacinta and Grijalva Rivers, ~ 1100 km and ~ 640 km long, respectively, are the longest rivers in Mexico, that discharges annually ~ 2678 m³s⁻¹, with peak discharges from July to November and rank second in fresh water discharge to the Gulf of Mexico (Day et al. 2003; Salas-de-León et al. 2008). These rivers originate from the northwestern part of the Guatemala and Chiapas (Mexico), respectively, and join together just ~ 50 km upstream the coast of the Gulf of Mexico (Armstrong-Altrin et al. 2017).

The Coatzacoalcos River originates from the Veracruz and Oaxaca States and drains between 17°46′N–92°25′W and 18°10′N–94°31′W. The Coatzacoalcos River lithofacies type consists of metasedimentary and volcanic rocks of the Oaxacan Complex. The Oaxacan Complex is located in the north of the Oaxaca State, which represents the most extensive outcrop of ~ 1 Ga basement in southern Mexico (~ 10,000 km²). It is composed of anorthosite, garnet-bearing charnockite, gabbros (U–Pb age of ~ 1230 Ma), diorite (~ 1012 Ma), and syenite

(~ 1130 Ma) (Solari et al. 2007). In general, the lithology of the Gulf of Mexico coastal area was dominated by alluvium (Quaternary), andesite and basalt (Cenozoic), sandstone and shale (Mesozoic), and schist and gneiss (Paleozoic) (Verma et al. 2016b) (Fig. 1).

4 Materials and methods

The 5.1 and 4.8-m-long sediment cores (GM6 and GM7) were recovered at 856 and 989 m water depth, respectively, at the southwestern Gulf of Mexico (Fig. 1). Forty samples at several intervals were selected for various analyses to deduce sediment provenance (Table 1).

Petrographic analysis was performed on 20 thin-sections to realize sediment composition. The grain-size and mineralogy were determined by Beckman Coulter particle size analyzer and Siemens D5000 X-ray Diffractometer (XRD), respectively, located at the Sedimentology Laboratory, Universidad Nacional Autónoma de México (UNAM). In addition, the chemistry of selected minerals was determined by a PHILLIPS XL-30 scanning electron microscope (SEM) equipped with energy dispersive spectrometer (EDS) at UNAM, Mexico.

For geochemical analysis, 20 g of 40 sediment samples were powdered (<62 μm) by an agate mortar. Bulk-sediment major-element concentrations were determined by X-ray fluorescence analysis (XRF) on fused

Table 2 ¹⁴C AMS ages for mixed planktic foraminifers

Core No.	Core section (cm)	Species	¹⁴C AMS age (yrs)	¹⁴C error (± year)	Calibrated age (cal yrs. BP)	Calibrated error (± year, 1 σ)
GM6	60–61	Mixed planktic foraminifers	2660	36	2388	51
	90–91		4400	36	4603	76
	150–151		7030	44	7544	43
	190–191		9170	44	10,021	85
	300–301		20,120	82	23,615	157
GM7	100–101		6790	44	7346	47
	210–211		16,190	73	19,007	218

Anaya-Gregorio *et al. Journal of Palaeogeography* (2018) 7:3

Page 4 of 19

glass beads at the geochemistry laboratory at UNAM, Mexico. The analytical accuracy is better than 5%. A detail about the analytical procedure and standards was described in Lozano and Bernal (2005). The trace and rare earth element concentrations were quantified using an inductively coupled plasma mass spectrometer (ICP-MS), following a methodology provided by Jarvis (1988). The accuracy, measured by an international standard BCR-2 was generally within 10%.

Samples for foraminiferal analysis were wet sieved through a 60 ASTM mesh (0.25 mm). Aliquots of the washed residues containing 300–500 foraminiferal individuals were analyzed through the microscope, and the specimens were taxonomically determined and counted. Separate fractions were used for benthic and planktic foraminifers. Benthic foraminifers were picked from the ≥63 μm fraction and planktonic from the ≥150 μm. Planktonic foraminifers were used to construct a biostratigraphic framework and benthics were analyzed for hypoxic characteristics.

Chronostratigraphic framework was achieved by ^{14}C dating on 20 micrograms of foraminiferal species *Globigerinoides ruber*, sent to Beta Analytics for accelerator

mass spectrometry (AMS) determination. The data were converted to calendar years with the CALIB program (Stuiver and Reimer 1993, version 502; http://calib.qub.ac.uk) (Table 2).

5 Results

5.1 Time framework

The time framework was elaborated based on seven ^{14}C dates, which was followed by the biostratigraphical scheme of Kennett and Huddlestun (1972) and Kennett et al. (1985). The bottom section of core GM6 reaches 23,615 cal yrs. BP (subzone Y2), with the limit of Pleistocene/Holocene at around 195 cm interval. Core GM7 bottom section revealed a ^{14}C age of about 19,007 cal yrs. BP, also fall within the subzone Y2. The Pleistocene/Holocene boundary is identified at 130 cm interval (Table 2, Fig. 2).

5.2 Granulometric analysis

The textural characteristics were studied at five intervals for the GM6 and GM7 cores (Table 1). The sediments are enriched in silt and clay contents, and poor in sand content in the cores GM6 (50.5 ± 1.67, 49.5 ± 1.67, and
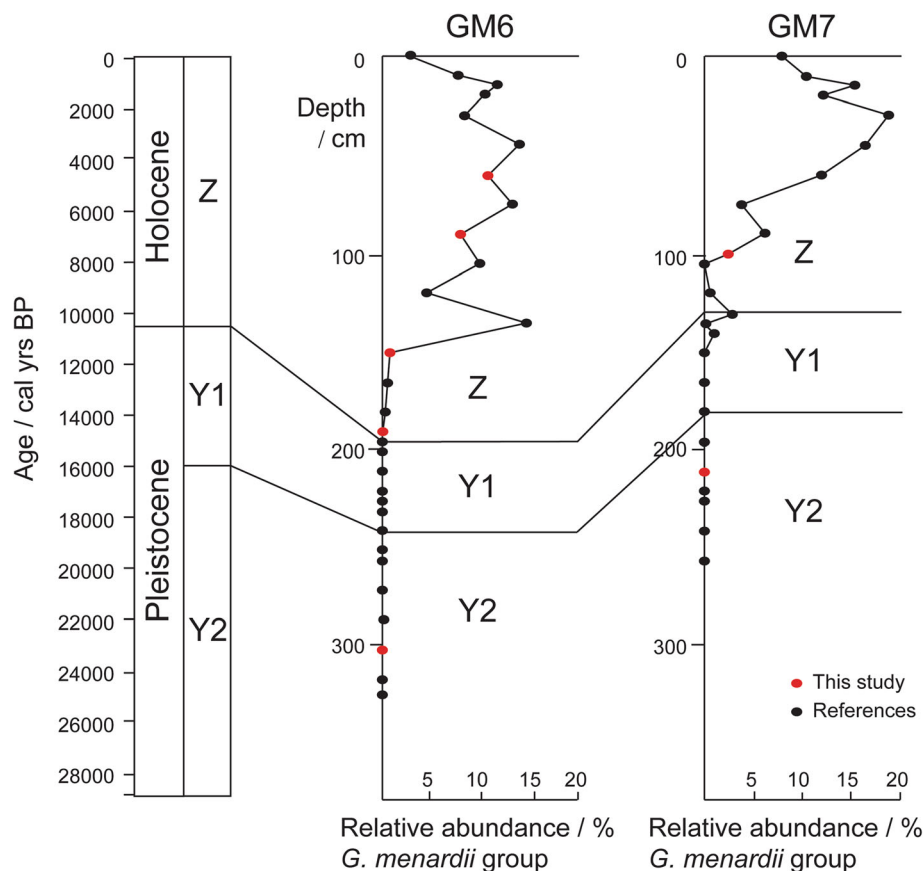

Fig. 2 Biostratigraphic correlation and ^{14}C ages (cal yrs. BP) for the sediment cores. The zone (Y) and sub-zones (Y1, and Y2) are based on the biostratigraphic classification of Kennett and Huddlestun (1972) and Kennett et al. (1985)

Anaya-Gregorio *et al. Journal of Palaeogeography* (2018) 7:3

Page 5 of 19

0.04 ± 0.05, respectively) and GM7 (49.7 ± 2.93, 50.3 ± 3.05, and 0.06 ± 0.13, respectively) (Table 1). The mean grain size (Mz) is similar for the GM6 and GM7 cores, which ranges from 7.99 φ to 8.13 φ and 7.80 φ to 8.17 φ, respectively, indicating that the sediments were dominated by silt and clay. The standard deviation values vary between 1.53–1.60 and 1.54–1.74 φ in the GM6 and GM7 cores, respectively, which reveal that the sediments are poorly sorted. The skewness (Sk$_1$) values vary between 0.02–0.05 and 0.02–0.07 φ for the GM6 and GM7 cores, respectively, indicating that the energy was constant during the deposition of sediments. The kurtosis (K$_G$) values of the GM6 and GM7 cores (0.92–0.94 and 0.93–0.95, respectively) indicate that the sediments are mesokurtic type (Table 1).
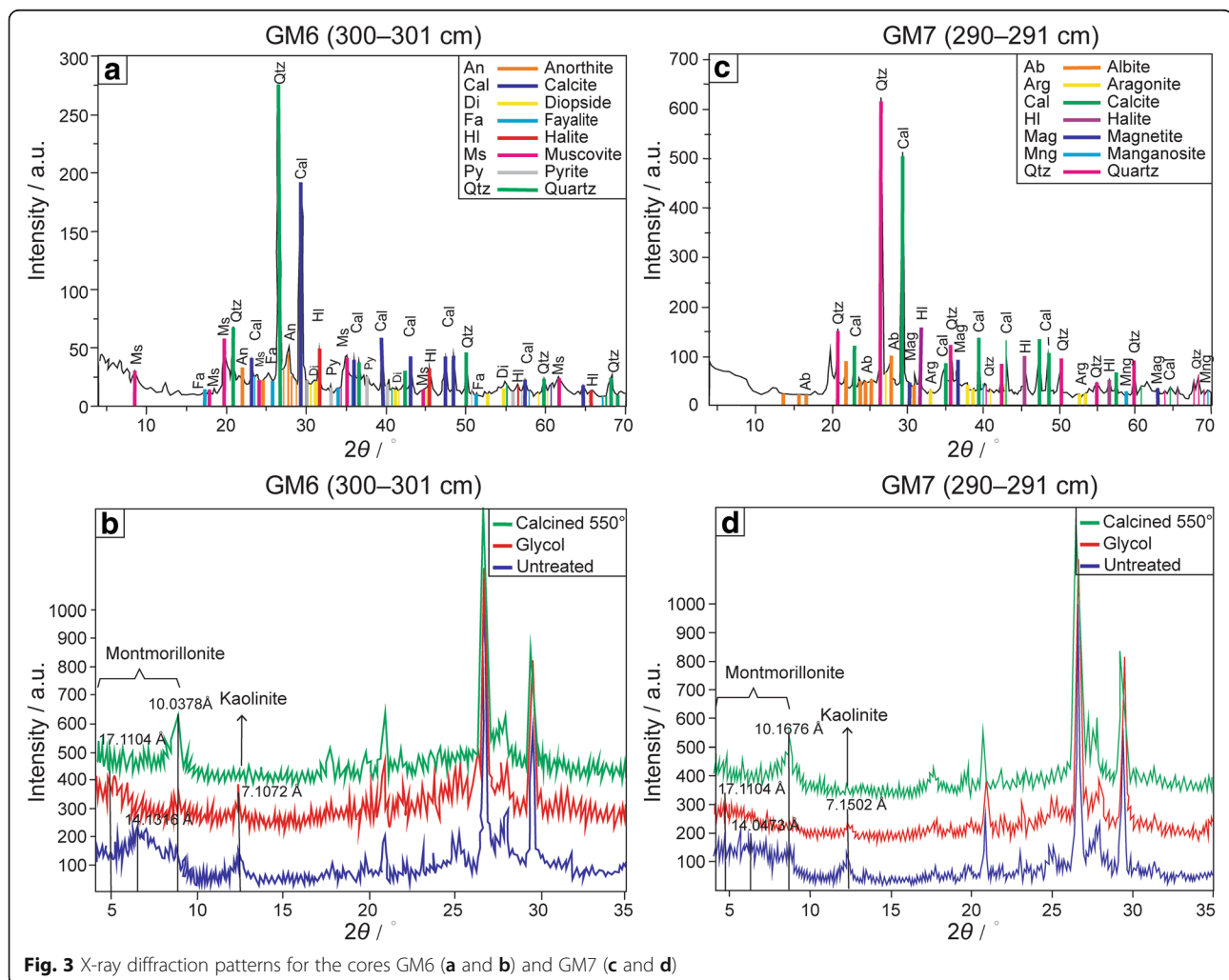
5.3 Mineralogy
The X-ray diffraction (XRD) data reveal that quartz and calcite are the major minerals, and muscovite, anorthite, halite, diopside, fayalite, and pyrite are the minor minerals in core GM6 (Fig. 3a; 300–301 cm interval; Last glacial
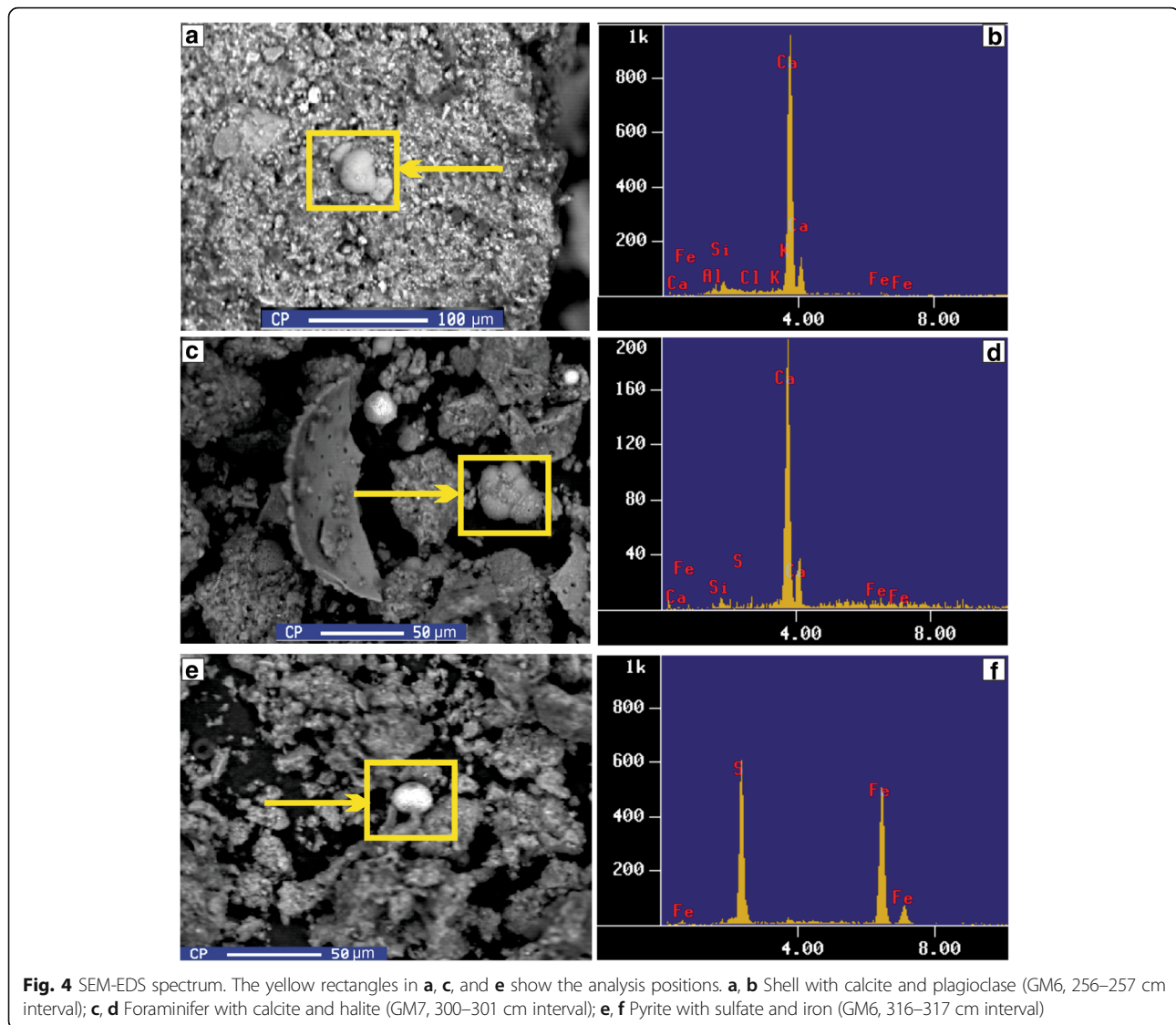
maximum, subzone Y2). On the other hand, in core GM7, quartz and calcite are identified as major, and halite, albite, magnetite, aragonite, and manganosite as minor minerals (Fig. 3c; 290–291 cm interval). Smectite and kaolinite are the dominant clay minerals in both cores (Fig. 3b and d).

The SEM energy dispersive spectrometer (SEM-EDS) analysis of sediments on selected intervals of the cores GM6 and GM7 reveals the concentration of minerals such as, plagioclase, halite, pyrite, and biogenic residues (Fig. 4). The minerals identified by SEM-EDS are consistent with the minerals identified by XRD method.

5.4 Major element concentrations
The variations in major element concentrations between the GM6 and GM7 cores, as well as its vertical distributions, are not statistically significant (Table 3). The upper continental crust (UCC; Taylor and McLennan 1985) normalized major element patterns in the two cores are similar, except MnO content, which is slightly higher in few samples at different intervals of cores GM6 and GM7 (Fig. 5).

Fig. 3 X-ray diffraction patterns for the cores GM6 (**a** and **b**) and GM7 (**c** and **d**)

Anaya-Gregorio *et al. Journal of Palaeogeography* (2018) 7:3

Page 6 of 19

Fig. 4 SEM-EDS spectrum. The yellow rectangles in **a**, **c**, and **e** show the analysis positions. **a**, **b** Shell with calcite and plagioclase (GM6, 256–257 cm interval); **c**, **d** Foraminifer with calcite and halite (GM7, 300–301 cm interval); **e**, **f** Pyrite with sulfate and iron (GM6, 316–317 cm interval)

The enrichment of MnO is probably due to the mineral manganosite. The Na_2O and K_2O contents in the cores GM6 and GM7 are depleted relative to UCC, indicating that the sediments are low in feldspar content (Nagarajan et al. 2017). The enrichment of Fe_2O_3 and TiO_2 contents is probably due to the presence of accessary minerals like magnetite and ilmenite, respectively (Papadopoulos et al. 2016). Geochemically, the sediments are classified mostly as shale (Fig. 6; Herron 1988).

5.5 Trace element concentrations
The trace element data for the GM6 and GM7 cores are listed in Table 4 and the UCC normalized patterns are illustrated in Fig. 7. The trace element contents between the GM6 and GM7 cores are almost similar, except Y and Zn. The Sc, Cr, Ni, and Cu contents in sediments

are low relative to those in UCC. The low concentrations of Rb, Ba, and U in the core sediments reveal its mobility during sedimentary processes (Feng and Kerrich 1992). The Zr and Hf contents, which represent detrital input, are depleted in core sediments relative to those in UCC. The correlations between Al_2O_3 and V, Cr, and Sc for the GM6 ($r = 0.38$, 0.38, and $– 0.19$, respectively; $n = 20$. r is correlation coefficient; the same follows) and GM7 ($r = 0.39$, 0.34, and 0.09, respectively; $n = 20$) cores are not statistically significant, indicating that these elements are not associated with aluminosilicates (Tzifas et al. 2017; Zaid 2015; Zaid et al. 2017).

5.6 Rare earth element concentrations
The variation in ΣREE contents in the cores GM6 (136–157 ppm) and GM7 (110–165 ppm) is statistically not significant (Table 5). The correlation between ΣREE and
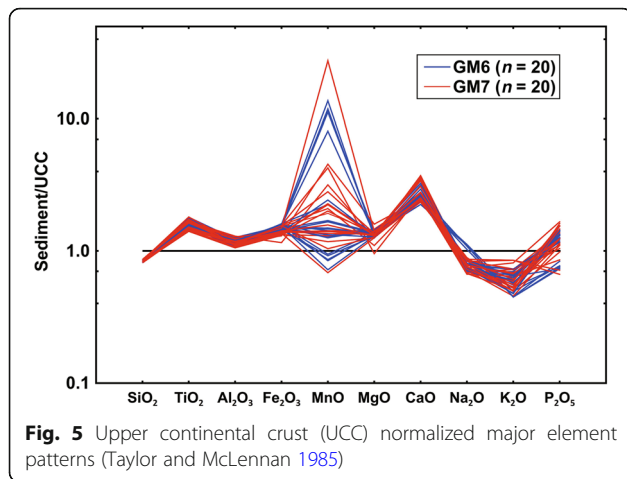
Table 3 Major element concentrations (weight %) for the deep sea sediments of the southwestern Gulf of Mexico

Core No.	GM6										
Section (cm)	0–1	31–32	46–47	61–62	76–77	91–92	121–122	136–137	151–152	166–167	180–181
vol. free SiO_2	56.2	55.9	54.6	54.2	54.7	54.8	55.1	53.9	53.7	54.9	54.5
SiO_2	45.7	45.3	44.1	44.1	45.5	45.2	44.8	44.1	43.8	46.0	44.7
TiO_2	0.617	0.645	0.612	0.689	0.626	0.651	0.714	0.624	0.653	0.625	0.656
Al_2O_3	14.2	13.9	14.0	15.6	14.8	14.4	14.9	13.9	14.7	15.0	14.3
$Fe_2O_3^*$	5.80	5.74	5.83	5.62	5.57	5.37	5.78	5.24	5.86	5.76	5.64
MnO	0.048	0.054	0.127	0.041	0.050	0.053	0.081	0.095	0.075	0.086	0.680
MgO	2.41	2.44	2.42	2.33	2.42	2.34	2.37	2.44	2.53	2.55	2.39
CaO	7.68	7.98	8.92	8.36	9.48	10.2	8.46	11.2	9.54	8.94	9.33
Na_2O	3.49	3.54	3.42	3.27	2.61	2.36	2.65	2.25	2.68	2.60	2.57
K_2O	1.24	1.36	1.23	1.25	1.86	1.67	1.46	1.69	1.57	2.06	1.54
P_2O_5	0.119	0.125	0.121	0.136	0.222	0.231	0.124	0.239	0.204	0.212	0.216
LOI	17.1	17.6	16.8	17.9	16.8	16.7	17.8	17.4	17.6	16.5	17.2
Sum	98.3	98.5	97.5	99.3	99.9	99.1	99.0	99.1	99.1	100.3	99.1
CIA	67	65	63	69	64	62	68	58	64	65	64
CIW	72	70	67	74	69	67	73	63	69	72	69
PIA	70	67	65	72	66	64	71	59	66	68	66
ICV	1.50	1.57	1.61	1.38	1.53	1.57	1.45	1.70	1.56	1.51	1.60
SiO_2/Al_2O_3	3.23	3.27	3.16	2.82	3.07	3.14	3.01	3.18	2.99	3.08	3.13
K_2O/Na_2O	0.354	0.383	0.359	0.382	0.711	0.708	0.549	0.748	0.587	0.795	0.598
Al_2O_3/Na_2O	4.05	3.91	4.09	4.79	5.67	6.09	5.62	6.15	5.47	5.76	5.54
K_2O/Al_2O_3	0.087	0.098	0.088	0.080	0.125	0.116	0.098	0.122	0.107	0.138	0.108

Section (cm)	196–197	210–211	222–223	226–227	241–242	256–257	300–301	316–317	330–331	Mean ± 1 s ($n = 20$)
vol. free SiO_2	55.5	55.5	54.9	53.7	55.0	53.9	54.5	55.1	53.6	54.7 ± 0.74
SiO_2	45.5	44.8	44.9	44.9	45.2	44.0	44.7	45.8	44.4	44.9 ± 0.67
TiO_2	0.635	0.638	0.623	0.625	0.647	0.613	0.631	0.612	0.745	0.64 ± 0.04
Al_2O_3	14.1	14.3	13.7	14.9	15.5	13.5	15.7	14.5	15.4	14.6 ± 0.66
$Fe_2O_3^*$	5.85	5.37	5.46	5.60	5.36	5.12	5.42	5.85	5.73	5.6 ± 0.23
MnO	0.785	0.096	0.076	1.835	0.086	0.139	0.074	0.470	0.650	0.28 ± 0.44
MgO	2.29	2.44	2.30	2.59	2.44	2.35	2.50	2.45	2.55	2.43 ± 0.09
CaO	8.25	8.79	10.8	8.39	8.76	11.7	8.86	9.06	8.97	9.18 ± 1.06
Na_2O	2.72	2.25	2.34	2.72	2.34	2.56	2.21	2.55	2.21	2.67 ± 0.43
K_2O	1.79	1.80	1.33	1.81	1.75	1.31	1.68	1.63	1.97	1.60 ± 0.25
P_2O_5	0.120	0.229	0.234	0.192	0.236	0.251	0.224	0.201	0.216	0.193 ± 0.05
LOI	15.6	17.7	17.8	16.3	17.6	18.0	17.5	17.2	17.2	17.2 ± 0.61
Sum	97.6	98.4	99.5	100.0	99.9	99.6	99.5	100.3	100.0	99.2 ± 0.82
CIA	65	65	59	67	68	56	69	65	67	65 ± 4
CIW	71	71	63	73	74	60	75	70	74	70 ± 4
PIA	69	68	61	71	72	57	73	68	71	67 ± 4
ICV	1.59	1.50	1.67	1.58	1.38	1.76	1.36	1.56	1.48	1.54 ± 0.10
SiO_2/Al_2O_3	3.24	3.14	3.27	3.01	2.93	3.25	2.84	3.16	2.87	3.09 ± 0.14
K_2O/Na_2O	0.659	0.800	0.568	0.665	0.748	0.512	0.760	0.639	0.888	0.621 ± 0.16
Al_2O_3/Na_2O	5.18	6.35	5.87	5.50	6.60	5.28	7.12	5.70	6.97	5.58 ± 0.09
K_2O/Al_2O_3	0.127	0.126	0.097	0.121	0.113	0.097	0.107	0.112	0.137	0.110 ± 0.016

Table 3 Major element concentrations (weight %) for the deep sea sediments of the southwestern Gulf of Mexico (Continued)

Core No.	GM7									
Section (cm)	0–1	31–32	46–47	61–62	76–77	91–92	121–122	136–137	151–152	166–167	180–181
vol. free SiO_2	54.6	55.0	54.0	55.0	54.8	54.1	53.5	54.9	56.5	54.4	56.0
SiO_2	45.7	44.9	43.7	45.8	45.7	43.8	43.6	45.3	47.3	44.3	45.9
TiO_2	0.605	0.670	0.570	0.680	0.604	0.571	0.585	0.621	0.680	0.618	0.740
Al_2O_3	15.0	15.9	13.7	15.7	14.4	13.2	13.4	14.0	14.8	14.4	14.7
$Fe_2O_3^*$	5.80	5.13	4.96	4.98	5.82	4.95	4.90	5.26	5.12	5.45	5.78
MnO	0.087	0.081	0.129	0.076	0.164	0.127	0.067	0.091	0.040	1.564	0.120
MgO	2.46	2.56	2.35	2.68	2.49	2.33	2.24	2.36	2.31	2.53	1.98
CaO	9.28	8.69	11.6	8.78	9.60	12.0	12.8	10.7	9.15	8.35	8.69
Na_2O	2.54	2.26	2.29	2.89	2.53	2.12	2.34	2.46	2.46	2.52	2.13
K_2O	2.06	1.26	1.47	1.48	1.90	1.63	1.37	1.40	1.58	1.44	1.79
P_2O_5	0.208	0.180	0.249	0.190	0.207	0.252	0.160	0.242	0.210	0.201	0.140
LOI	16.0	18.0	19.0	16.7	17.2	18.5	18.5	16.9	16.2	17.5	17.6
Sum	99.8	99.6	100.0	99.9	100.7	99.4	100.0	99.5	99.8	98.9	99.5
CIA	64	71	57	68	63	55	54	60	66	68	67
CIW	71	76	61	73	68	59	57	64	71	72	73
PIA	68	74	58	71	65	56	55	62	68	70	70
ICV	1.52	1.30	1.71	1.38	1.60	1.80	1.80	1.63	1.44	1.56	1.45
SiO_2/Al_2O_3	3.04	2.83	3.20	2.92	3.17	3.33	3.24	3.23	3.20	3.07	3.13
K_2O/Na_2O	0.812	0.558	0.643	0.512	0.752	0.766	0.585	0.570	0.642	0.573	0.840
Al_2O_3/Na_2O	5.92	7.02	5.98	5.43	5.70	6.20	5.74	5.71	6.01	5.72	6.88
K_2O/Al_2O_3	0.137	0.079	0.108	0.094	0.132	0.124	0.102	0.100	0.107	0.100	0.122
Section (cm)	196–197	210–211	222–223	226–227	241–242	256–257	300–301	316–317	330–331	Mean ± 1 s (n = 20)	
vol. free SiO_2	55.3	56.0	54.5	55.0	55.0	55.3	55.5	56.9	55.4	55.1 ± 0.83	
SiO_2	46.7	47.0	44.3	45.0	44.7	45.3	45.4	47.7	45.2	45.4 ± 1.16	
TiO_2	0.625	0.730	0.572	0.593	0.680	0.690	0.690	0.725	0.620	0.643 ± 0.056	
Al_2O_3	14.9	14.3	13.0	14.7	16.0	13.6	14.4	14.3	15.1	14.5 ± 0.84	
$Fe_2O_3^*$	5.87	5.91	4.79	5.20	4.23	5.12	4.79	5.84	5.06	5.25 ± 0.46	
MnO	0.114	0.250	0.114	0.081	0.180	0.078	0.260	0.061	0.080	0.188 ± 0.33	
MgO	2.59	1.76	2.39	2.36	2.25	2.41	2.87	2.36	2.49	2.39 ± 0.24	
CaO	8.53	9.46	12.3	8.69	8.36	9.56	8.49	8.26	8.37	9.58 ± 1.45	
Na_2O	2.82	2.24	2.14	2.76	2.36	2.65	2.68	2.73	2.49	2.47 ± 0.23	
K_2O	2.06	2.06	1.39	2.36	2.24	2.36	2.03	1.74	1.89	1.78 ± 0.35	
P_2O_5	0.188	0.230	0.262	0.109	0.270	0.117	0.190	0.188	0.170	0.198 ± 0.045	
LOI	16.1	16.0	18.1	15.7	18.0	16.8	17.5	14.9	18.4	17.2 ± 1.11	
Sum	100.5	99.9	99.3	97.6	99.2	98.6	99.2	98.8	99.8	99.5 ± 0.68	
CIA	66	63	54	64	69	59	65	66	68	63 ± 5	
CIW	72	69	58	71	77	66	71	72	74	69 ± 6	
PIA	69	66	55	68	74	61	68	69	72	66 ± 6	
ICV	1.51	1.57	1.82	1.50	1.27	1.68	1.52	1.52	1.39	1.55 ± 0.16	
SiO_2/Al_2O_3	3.13	3.29	3.40	3.06	2.80	3.33	3.15	3.34	2.99	3.14 ± 0.17	
K_2O/Na_2O	0.729	0.920	0.651	0.857	0.949	0.891	0.757	0.637	0.759	0.72 ± 0.13	
Al_2O_3/Na_2O	5.30	6.37	6.10	5.34	6.77	5.12	5.37	5.23	6.07	5.90 ± 0.55	
K_2O/Al_2O_3	0.138	0.144	0.107	0.160	0.140	0.174	0.141	0.122	0.125	0.123 ± 0.174	

Abbreviations: *1 s*-One standard deviation, *n* Total number of samples, *LOI* Loss of ignition, *CIA* Chemical index of alteration (Nesbitt and Young 1982), *CIW* Chemical index of weathering (Harnois 1988), *PIA* Plagioclase index of alteration (Fedo et al. 1995), *ICV* Index of compositional variability (Cox et al. 1995), $Fe_2O_3^*$ Total Fe expressed as Fe_2O_3. Refer to Table 1, for water depth, latitude and longitude

Anaya-Gregorio *et al. Journal of Palaeogeography* (2018) 7:3

Page 9 of 19

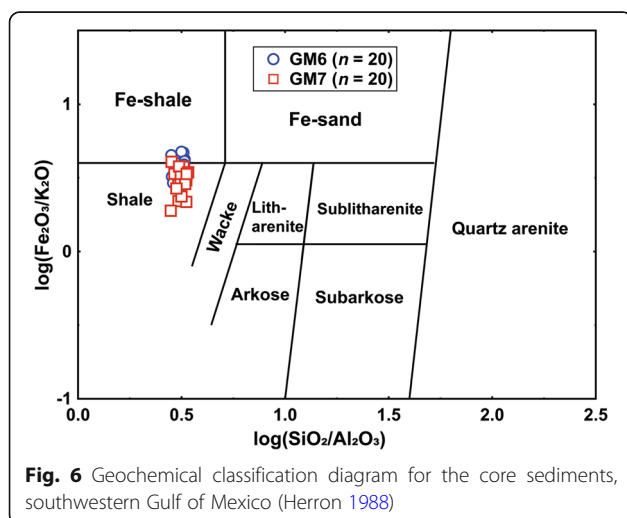**Fig. 5** Upper continental crust (UCC) normalized major element patterns (Taylor and McLennan 1985)

Zr contents is positive for the GM6 ($r = 0.57$, $n = 20$) and GM7 ($r = 0.45$, $n = 20$) cores. On the other hand, the correlation between ΣREE and Al_2O_3 is negative for the GM6 ($r = -0.14$, $n = 20$) and GM7 ($r = -0.15$, $n = 20$) cores, which indicates that the REE contents are housed in accessory mineral like zircon (Armstrong-Altrin et al. 2012; Periasamy and Venkateshwarlu 2017; Wang et al. 2017c, 2017d). The North American shale composite (NASC) normalized REE patterns for the GM6 and GM7 cores are characterized by flat light REE (LREE) and enriched heavy REE (HREE) with negative and positive Eu anomalies (Fig. 8). However, the Eu anomalies in cores GM6 (Eu/Eu* = 0.892 to 1.03) and GM7 (Eu/Eu* = 0.887 to 1.14) are similar (Table 5).

6 Discussion

6.1 Palaeoweathering indices and sediment recycling

The chemical composition of detrital sediments is highly useful to interpret the intensity of weathering as well as sediment recycling (Tawfik et al. 2017). Although huge

Fig. 6 Geochemical classification diagram for the core sediments, southwestern Gulf of Mexico (Herron 1988)

number of weathering indices was proposed by various authors, in this study, we preferred the most commonly used weathering indices like CIA (Nesbitt and Young 1982), CIW (Harnois 1988), and PIA (Fedo et al. 1995). These weathering indices are represented by the following equations: CIA = $[Al_2O_3/(Al_2O_3 + CaO^* + Na_2O + K_2O)] \times 100$, CIW = $[Al_2O_3/Al_2O_3 + CaO^* + Na_2O] \times 100$, and PIA = $[Al_2O_3 - K_2O/(Al_2O_3 + CaO^* + Na_2O)] \times 100$, in which CaO* represents CaO only incorporated in the silicate fraction. The Ca content in the silicate fraction was calculated by the equation: Ca = $CaO_t - CaO_{trg}$ and $CaO_{trg} = (Al_2O_3)_t \times (CaO/Al_2O_3)_{UCC}$, where "t" = the total abundance in the sample and "trg" = terrigenous.

The CIA, CIW, and PIA values increase if weathering increases and values of ≤50 indicate low weathering (Fedo et al. 1995; Harnois 1988; Nesbitt and Young 1982). The CIA and CIW values for the GM6 core vary from 56 to 69 and from 60 to 75, respectively, and for GM7, which vary from 54 to 71 and from 57 to 77, respectively (Table 3). Similarly, the PIA values for the core GM6 vary from 57 to 73 and for core GM7, which vary between 55 and 74 (Table 3). The CIA, CIW, and PIA values of the core sediments are indicating a moderate to intense weathering condition (Table 3). On the other hand, index of compositional variability (ICV = $[(CaO + K_2O + Na_2O + Fe_2O_3^{(t)} + MgO + MnO + TiO_2)/Al_2O_3]$; Cox et al. 1995), where $Fe_2O_3^{(t)}$ represents total iron, is another method commonly used to infer sediment recycling, which decreases when weathering increases (Armstrong-Altrin et al. 2014, 2017; Madhavaraju et al. 2017; Nagarajan et al. 2017). According to Cox et al. (1995), the ICV value is high (>1) in little-weathered detrital minerals like pyroxene and feldspar and it is low (<1) in highly-weathered fine-grained sediments like clay. The ICV values for the core sediments GM6 (1.36–1.76) and GM7 (1.27–1.82) reveal a moderate weathering intensity in the source area (Table 3).

The elemental ratios such as SiO_2/Al_2O_3, Al_2O_3/Na_2O, and K_2O/Na_2O have been used extensively by various authors to interpret sediment recycling and are considered as a proxy to infer detrital input (Armstrong-Altrin 2009; Madhavaraju et al. 2016; Zaid 2013; Zaid et al. 2015). These ratios are >6, >5, and >1, respectively, if the sediment recycling is high (Tapia-Fernandez et al. 2017). The SiO_2/Al_2O_3, Al_2O_3/Na_2O, and K_2O/Na_2O ratios of the cores GM6 (2.82–3.27, 4–7, and 0.354–0.888, respectively) and GM7 (2.8–3.4, 5–7, and 0.512–0.949, respectively) are indicating low to moderate sediment recycling.

6.2 Sediment provenance

The provenance discrimination diagram of Roser and Korsch (1988) is widely preferred by various researchers to infer sediment provenance (Armstrong-Altrin 2009; Hernández-Hinojosa et al. 2018; Nagarajan et al. 2017; Tapia-Fernandez et al. 2017). The discrimination diagram

Anaya-Gregorio *et al. Journal of Palaeogeography* (2018) 7:3

Page 10 of 19

Table 4 Trace element concentrations (ppm) for the deep sea sediments of the southwestern Gulf of Mexico

Core No.	GM6										
Section (cm)	0–1	31–32	46–47	61–62	76–77	91–92	121–122	136–137	151–152	166–167	180–181
Ba	378	425	339	385	301	360	365	369	435	380	465
Co	26.2	25.5	22.1	23.7	18.9	23.6	24.8	21.9	19	22.8	21.7
Cr	73.1	75.6	78.6	81.7	69.1	88.1	85.5	79.6	79.9	81.8	76.9
Cs	7.4	5.64	7.89	5.78	7.31	7.93	6.54	7.22	4.89	8.32	4.79
Cu	22.5	22.8	23	22.6	19.9	22.8	21.8	20.1	20.8	21.8	22.9
Hf	3.31	3.21	3.45	3.45	2.99	3.64	2.98	3.42	3.16	3.21	3.07
Mo	6.62	1.2	1.4	1.4	0.737	1	1.1	0.755	1.3	0.853	1.4
Nb	12.5	10.5	13.5	11.8	11.8	13.6	12.6	13	12.5	13.4	12.7
Ni	23	23.5	21.7	23.8	18	21.4	24.6	21.3	25	17.8	26
Pb	24.8	15.9	24	17.9	16.2	15	16.4	14.1	17.9	16	14.8
Rb	100	99.5	102.1	98.7	92.1	107	102.5	94	86.8	107.1	103.5
Sc	14.1	12.7	15.3	14.6	12.9	15.3	13.8	14	12.9	14.8	10.8
Sr	322.6	389.2	379.7	356.4	318.9	496.9	310.8	523.7	376.9	357.8	365.5
Ta	0.449	0.436	0.497	0.48	0.45	0.401	0.86	0.497	1.25	0.447	0.75
Th	10.1	9.87	10.4	8.65	9.66	10.2	6.78	10	7.45	10.3	8.65
U	2.25	2.89	2.25	2.47	2.63	4.19	2.78	3.11	2.63	2.73	2.78
V	116.6	118.4	119.4	112.8	115.1	118.9	135.6	107	117.7	124.7	129.5
Y	22.2	25.6	24.1	9.85	21.1	25.4	19.6	24.2	18.7	24.2	8.39
Zn	375.1	77.7	47.9	89.7	20	26	78.6	19	79.7	22	68.5
Zr	119.2	88.7	133	79.7	109.4	138	96.3	127.7	112.4	126.8	102.5
V/Cr	1.60	1.57	1.52	1.38	1.67	1.35	1.59	1.34	1.47	1.52	1.68
Ni/Co	0.88	0.92	0.98	1.00	0.95	0.91	0.99	0.97	1.32	0.78	1.20
Cu/Zn	0.06	0.29	0.48	0.25	1.00	0.88	0.28	1.06	0.26	0.99	0.33
U_{au}	−1.10	−0.40	−1.21	−0.41	−0.59	0.80	0.52	−0.23	0.15	−0.69	−0.10
Section (cm)	196–197	210–211	222–223	226–227	241–242	256–257	300–301	316–317	330–331	Mean ± 1 s (*n* = 20)	
Ba	359	336	360	378	287	355	276	385	379	366 ± 46	
Co	21.5	24.4	22.5	19.3	23.8	21.3	29	20.9	19.6	22.6 ± 2.59	
Cr	67.6	84.5	77.5	62.8	94.8	70.7	92.7	71.8	84.7	78.8 ± 8.28	
Cs	7.5	6.92	6.95	7.05	6.78	7.12	6.35	8.02	5.84	6.81 ± 1.00	
Cu	21.1	20.9	21.4	18.2	23.7	19.9	19.9	21.6	22	21.5 ± 1.39	
Hf	3.31	3.07	3.13	3.06	3.02	3.27	3.18	3.33	3.45	3.24 ± 0.18	
Mo	4.51	0.727	0.91	0.261	1.3	0.712	1.4	1.52	1.8	1.55 ± 1.46	
Nb	12.6	12.5	12.1	9	13.1	12.9	13.5	13.3	13.8	12.5 ± 1.13	
Ni	21.5	26.3	27.9	13.6	27.9	18.8	28.5	16.2	28.8	22.8 ± 4.3	
Pb	22.8	13.8	13.4	15	22.8	14	24.7	18.8	25.7	18.2 ± 4.26	
Rb	95.4	93.6	95.3	88.4	101.5	96.4	99.9	106	102.7	98.6 ± 5.78	
Sc	13.9	14.3	12.9	12.2	11.9	12.6	12.4	14.1	10.5	13.3 ± 1.35	
Sr	330.2	525.1	463	311.5	366.8	534.5	325.5	359.6	371.9	389 ± 76	
Ta	0.51	0.445	0.353	0.145	0.46	0.46	0.56	0.393	0.54	0.52 ± 0.22	
Th	10.1	9.49	9.21	9.97	9.45	9.92	9.78	10.4	10.5	9.54 ± 0.98	
U	2.05	3.04	3.09	1.95	3.12	2.61	3.14	2.09	3.25	2.75 ± 0.52	
V	118.2	107.6	108.4	94.1	136.5	101.1	139.5	117.6	140.6	119 ± 13	
Y	22.2	23.2	22.7	20.2	10.4	23.7	27.7	23.7	8.65	20.3 ± 6.02	

Table 4 Trace element concentrations (ppm) for the deep sea sediments of the southwestern Gulf of Mexico *(Continued)*

Zn	51.1	38.9	25	20	43.3	23	60.4	26	126.5	65.9 ± 78.5
Zr	118.5	117.5	121.3	105.8	99.7	122.1	78.6	126.1	102.4	111 ± 17
V/Cr	1.75	1.27	1.40	1.50	1.44	1.43	1.50	1.64	1.66	1.51 ± 0.13
Ni/Co	1.00	1.08	1.24	0.70	1.17	0.88	0.98	0.78	1.47	1.01 ± 0.19
Cu/Zn	0.41	0.54	0.86	0.91	0.55	0.87	0.33	0.83	0.17	0.57 ± 0.32
U_{au}	−1.33	−0.12	0.03	−1.37	−0.03	−0.70	−0.12	−1.38	−0.23	−0.42 ± 0.62

Core No.	GM7										
Section (cm)	0–1	31–32	46–47	61–62	76–77	91–92	121–122	136–137	151–152	166–167	180–181
Ba	336	325	421	358	371	375	394	348	423	430	414
Co	18.8	19.4	21.5	16.6	20.1	17.5	20.8	19.2	21.5	24.3	22.4
Cr	65	75.4	66.9	78.5	70.3	42.8	69.8	59.8	79.8	69.4	82.6
Cs	7.21	6.89	7.38	6.45	7.92	6.55	6.67	6.49	6.87	7.61	7.36
Cu	18.7	19.6	20.1	20.5	20.5	17.8	20	18.3	23.5	21.6	19.7
Hf	3.17	2.78	3.36	2.65	3.27	3.05	3.1	3.06	3.26	3.16	3.45
Mo	0.736	0.756	0.746	0.814	0.864	0.752	0.745	0.71	0.478	0.267	0.642
Nb	11.3	13.5	13.4	10.7	12.9	10.9	12.6	10.6	14.6	13.1	13.8
Ni	13.6	33.6	18.4	28.6	15.5	19	21.3	15.9	34.2	15.8	31.6
Pb	17.5	14.9	14.3	17	17.6	13.7	13.2	13.2	16.4	17.6	13.5
Rb	93.7	95.7	97.7	78.6	104.2	88.1	90.6	87.9	81.7	99.7	79.4
Sc	12.3	11.7	13.2	12.5	13.6	11.6	13.2	11.2	13.7	13.8	11.5
Sr	318.6	456.4	523.6	478.3	371.2	500.7	557.9	403.5	298.5	353.6	345.7
Ta	0.405	1.25	0.509	0.69	0.419	0.374	0.465	0.324	0.56	0.433	0.48
Th	10.1	11.7	10.6	9.58	10.5	9.86	9.5	9.02	9.68	9.88	9.48
U	2.04	2.31	3.12	2.18	2.07	2.69	2.73	3.24	2.64	1.95	2.16
V	103.9	125.4	104.8	140.3	118.1	84.8	99.1	95	98.6	112.7	175.6
Y	20.6	28.7	23.4	23.5	23	21.1	22.6	20.3	21.5	22.9	20.7
Zn	23.1	42.4	21	41.6	25	20	20	34.6	19.6	23	18.5
Zr	105.3	110.6	124.3	14.8	120.3	107.6	118.5	108.9	99.6	121.4	125.6
V/Cr	1.60	1.66	1.57	1.79	1.68	1.98	1.42	1.59	1.24	1.62	2.13
Ni/Co	0.72	1.73	0.86	1.72	0.77	1.09	1.02	0.83	1.59	0.65	1.41
Cu/Zn	0.81	0.46	0.96	0.49	0.82	0.89	1.00	0.53	1.20	0.94	1.06
U_{au}	−1.31	−1.57	−0.41	−1.01	−1.43	−0.60	−0.43	0.23	−0.59	−1.34	−1.00

Section (cm)	196–197	210–211	222–223	226–227	241–242	256–257	300–301	316–317	330–331	Mean ± 1 s (*n* = 20)
Ba	379	426	327	352	387	349	315	399	325	373 ± 38
Co	21.7	24.7	16	19.5	27.9	14.9	28.6	27.5	29.5	21.6 ± 4.27
Cr	77.3	74.7	57.5	69.6	68.6	51.3	71.9	108.6	75	70.7 ± 13.2
Cs	8.43	5.64	6.45	7.82	4.35	6.59	3.65	7.29	3.12	6.54 ± 1.39
Cu	22.2	19.8	16.9	21.4	21.6	20.2	22.3	24.3	21.5	20.5 ± 1.85
Hf	3.43	2.78	2.94	3.27	2.86	3.2	2.76	3.66	3.15	3.12 ± 0.26
Mo	0.888	0.812	0.679	0.969	0.843	1.24	0.972	0.973	0.856	1.21 ± 1.09
Nb	14.2	13.8	11.5	12.8	14.6	12.6	13.8	15.4	13.3	13.0 ± 1.37
Ni	17.1	29.8	24.3	21.6	35.4	20.1	39.8	29.5	32.1	24.8 ± 7.99
Pb	16.8	14.4	13.3	16.8	16.8	25.9	17.6	15.8	18.7	16.2 ± 2.88
Rb	107.2	83.6	88.8	100.9	92.5	90.5	98.6	100.6	97.7	93 ± 8.2
Sc	15.4	12.9	10.1	14.1	13.7	11.3	11.8	19.2	12.6	13 ± 1.9

Anaya-Gregorio *et al. Journal of Palaeogeography* (2018) 7:3

Page 12 of 19

Table 4 Trace element concentrations (ppm) for the deep sea sediments of the southwestern Gulf of Mexico *(Continued)*

Sr	347.4	412.4	561.4	335	432.5	350.6	416.4	459.1	468.4	420 ± 79
Ta	0.518	1.65	0.381	0.504	0.68	0.512	0.46	0.526	0.47	0.58 ± 0.32
Th	10.6	10.7	9.56	10.3	8.49	9.88	10.8	10.6	9.34	10 ± 0.72
U	2.44	2.34	2.75	2.95	2.17	2.67	2.62	3.07	2.49	2.53 ± 0.38
V	122.3	123.5	87.5	116	118.6	101.6	137.6	153.6	103.5	116 ± 23
Y	24.8	21.8	21	22.7	21.6	22.9	22.8	26.7	23.9	22.8 ± 2.07
Zn	53	26.5	42.8	263.8	43.6	38.2	69.8	50.6	57.4	47 ± 53
Zr	133	134.3	101.2	118.4	89.5	101.8	110.5	152.8	114.3	111 ± 27
V/Cr	1.58	1.65	1.52	1.67	1.73	1.98	1.91	1.41	1.38	1.66 ± 0.22
Ni/Co	0.79	1.21	1.52	1.11	1.27	1.35	1.39	1.07	1.09	1.16 ± 0.33
Cu/Zn	0.42	0.75	0.39	0.08	0.50	0.53	0.32	0.48	0.37	0.65 ± 0.30
U_{au}	−1.08	−1.21	−0.44	−0.47	−0.66	−0.62	−0.97	−0.45	−0.62	-0.80 ± 0.44

Refer to Table 1, for water depth, latitude and longitude. Authigenic uranium U_{au} = Total U − Th/3

of Roser and Korsch (1988) reveals that the sediments from the cores GM6 and GM7 were derived by the weathering of intermediate source rocks like basaltic andesite (Fig. 9). Similarly, the bivariate diagram based on La/Sc and Co/Th ratios also suggests that the sediments were most probably derived from an intermediate source rock (Fig. 10).

The characteristics of the REE pattern and the Eu anomaly can be used as a tool to infer sediment provenance (Cullers et al. 1997). The REE patterns of the GM6 and GM7 core sediments are enriched in LREE and depleted in HREE with low negative to positive Eu anomalies, suggesting the derivation of sediments from an intermediate igneous rock. Furthermore, we compared the chondrite-normalized REE patterns of the core sediments with the potential source rocks from the southern Gulf of Mexico (Fig. 11). This comparison again demonstrates that the intermediate rocks as the probable source rocks for the two sediment cores, which is consistent with the geology of the Gulf of Mexico (Fig. 1).
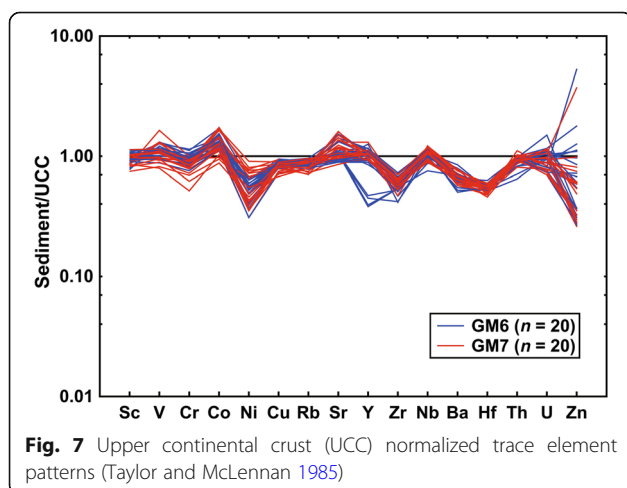

Fig. 7 Upper continental crust (UCC) normalized trace element patterns (Taylor and McLennan 1985)

6.3 Redox-sensitive trace element concentrations

Among other REEs, cerium (Ce) is sensitive to changes in redox conditions, so its depletion or enrichment can report changes in the oxygenation conditions of a depositional medium (Elderfield and Greaves 1982). A positive Ce anomaly (Ce/Ce* ≥ 1) in sediments suggests its deposition under an anoxic condition, whereas a negative Ce anomaly (Ce/Ce* < 1) represents an oxic condition (Tostevin et al. 2016). In this study, negative Ce anomaly (Ce/Ce* < 1) is observed, which varies from 0.845 to 0.907 and from 0.84 to 0.986 for the GM6 and GM7 cores, respectively, indicating an oxic depositional condition (Table 5).

The V/Cr ratio is considered as a good indicator of a redox condition, if this ratio is >4.5, which represents an anoxic condition, whereas <2 indicates an oxic condition in the depositional environment (Jones and Manning 1994). The V/Cr ratio in the GM6 (1.27–1.75) and GM7 (1.24 to 1.98, except one sample with value 2.13) cores are <2 (Table 4), indicating an oxic condition. In addition, Ni/Co ratio <5 and >5 indicate oxic and anoxic conditions, respectively (Jones and Manning 1994). The Ni/Co ratios for the GM6 and GM7 cores range from 0.70 to 1.47 and from 0.65 to 1.73, respectively, indicating an oxic condition. Similarly, the Cu/Zn ratio is also a good paleo-redox indicator, which is always high (>1) in the redox depositional condition (Goldberg and Humayun 2016). The Cu/Zn ratios in the GM6 and GM7 core sediments are <1 (0.57 ± 0.32 and 0.65 ± 0.30, respectively), indicating an oxic condition. Wignall and Myers (1988) documented that the authigenic uranium (U_{au} = Total U − Th/3) values between 5 and 12 suggest an oxic depositional condition, whereas values >12 are indicative of suboxic and anoxic conditions. The authigenic uranium values in GM6 core range from − 1.38 to 0.620 and for the GM7 core, they vary from − 1.57 to 0.231, suggesting an oxic depositional condition.

Anaya-Gregorio *et al. Journal of Palaeogeography* (2018) 7:3

Page 13 of 19

Table 5 Rare earth element concentrations (ppm) for the deep sea sediments of the Southwestern Gulf of Mexico

Core No.	GM6										
Section (cm)	0–1	31–32	46–47	61–62	76–77	91–92	121–122	136–137	151–152	166–167	180–181
La	30.3	28.7	32.9	30.5	29.5	33.4	31.3	32.3	30.7	33.4	29.8
Ce	60.4	59.6	64.8	58.5	57.7	64.3	59.4	60.7	57.6	65	58.8
Pr	7.3	7.15	7.95	7.26	7.11	8	7.45	7.58	6.74	7.93	6.89
Nd	26.1	26.1	28.5	25.5	25.5	28.7	26.9	27.7	25.9	28.4	26.3
Sm	5.31	5.26	5.71	5.25	5.02	5.68	5.14	5.48	5.25	5.52	5.24
Eu	1.03	1.15	1.15	1.03	1.01	1.2	1.04	1.14	1.06	1.14	1.07
Gd	4.49	4.52	4.83	4.79	4.32	4.95	4.65	4.86	4.24	4.88	4.58
Tb	0.717	0.725	0.764	0.745	0.685	0.785	0.736	0.772	0.715	0.758	0.726
Dy	3.96	3.95	4.2	3.9	3.79	4.28	3.77	4.08	3.77	4.12	3.78
Ho	0.821	0.834	0.828	0.813	0.769	0.862	0.808	0.843	0.775	0.822	0.789
Er	2.14	2.12	2.23	2.13	2.02	2.31	2.14	2.23	2.13	2.18	2.18
Tm	0.31	0.311	0.334	0.301	0.305	0.325	0.291	0.33	0.295	0.316	0.308
Yb	2	1.98	2.17	1.95	1.98	2.24	1.96	2.17	1.95	2.16	1.98
Lu	0.303	0.301	0.324	0.302	0.294	0.32	0.291	0.32	0.29	0.324	0.31
LREE	129	127	140	127	125	140	130	134	126	140	127
HREE	14.7	14.7	15.7	14.9	14.2	16.1	14.6	15.6	14.2	15.6	14.7
ΣREE	145	143	157	143	140	157	146	151	141	157	143
Eu/Eu*	0.93	1.03	0.958	0.898	0.952	0.991	0.934	0.967	0.982	0.968	0.959
Ce/Ce*	0.885	0.907	0.873	0.855	0.868	0.856	0.848	0.845	0.871	0.87	0.893
Section (cm)	196–197	210–211	222–223	226–227	241–242	256–257	300–301	316–317	330–331	Mean ± 1 s (*n* = 20)	
La	30.8	31.2	30.2	29	31.6	31.8	30.5	33.1	31.8	31.1 ± 1.40	
Ce	60.4	59.1	57.3	55.1	60.5	60.1	60.2	65.2	60.5	60.3 ± 2.73	
Pr	7.36	7.35	7.05	6.94	7.24	7.49	7.56	7.93	7.38	7.38 ± 0.36	
Nd	26.3	26.7	25.4	24.8	26.6	26.8	27.5	28.2	27.5	26.8 ± 1.14	
Sm	5.26	5.28	5.01	4.96	5.21	5.35	5.28	5.52	5.26	5.30 ± 0.20	
Eu	1.06	1.08	1.06	0.98	0.96	1.13	1.06	1.1	1.04	1.07 ± 0.06	
Gd	4.59	4.61	4.5	4.22	4.26	4.92	4.35	4.75	4.38	4.58 ± 0.24	
Tb	0.733	0.718	0.705	0.67	0.715	0.75	0.715	0.752	0.735	0.73 ± 0.03	
Dy	3.94	3.9	3.82	3.77	3.76	4.11	3.81	4.13	3.79	3.93 ± 0.17	
Ho	0.811	0.796	0.782	0.747	0.836	0.828	0.802	0.835	0.815	0.81 ± 0.03	
Er	2.12	2.1	2.06	2	2.11	2.14	2.12	2.28	2.09	2.14 ± 0.08	
Tm	0.313	0.306	0.3	0.297	0.291	0.315	0.31	0.318	0.309	0.31 ± 0.01	
Yb	2.1	2.02	1.99	1.98	2.01	2.15	2.01	2.15	2.03	2.05 ± 0.09	
Lu	0.307	0.301	0.299	0.297	0.302	0.31	0.301	0.317	0.303	0.31 ± 0.01	
LREE	130	130	125	121	131	132	131	140	132	131 ± 5.61	
HREE	14.9	14.8	14.5	14.0	14.3	15.5	14.4	15.5	14.5	14.9 ± 0.60	
ΣREE	146	145	140	136	146	148	146	157	148	147 ± 6.16	
Eu/Eu*	0.945	0.962	0.98	0.935	0.892	0.968	0.974	0.942	0.945	0.956 ± 0.031	
Ce/Ce*	0.875	0.85	0.855	0.845	0.869	0.848	0.865	0.877	0.86	0.866 ± 0.017	
Core No.	GM7										
Section (cm)	0–1	31–32	46–47	61–62	76–77	91–92	121–122	136–137	151–152	166–167	180–181
La	29.2	26.5	33.3	24.6	32.4	29.5	31.2	27.3	30.5	32	23.2
Ce	57.1	53.3	63.3	50.2	63.4	55.3	59	52.3	61.9	62.3	49.8

Anaya-Gregorio *et al. Journal of Palaeogeography* (2018) 7:3

Page 14 of 19

Table 5 Rare earth element concentrations (ppm) for the deep sea sediments of the Southwestern Gulf of Mexico *(Continued)*

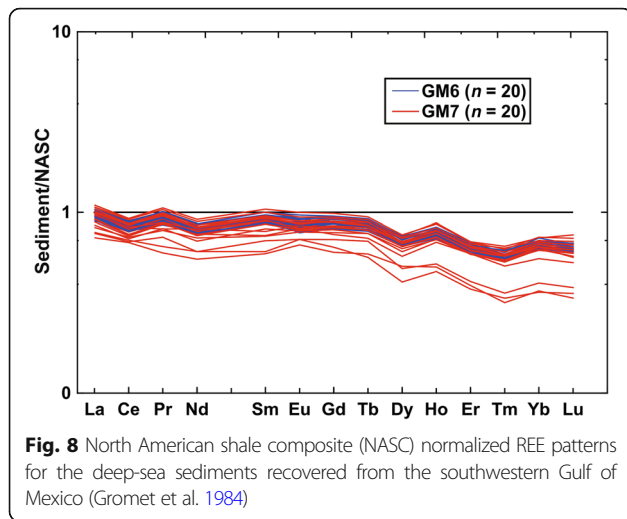| Pr	6.96	6.28	7.85	5.76	7.72	6.87	7.28	6.43	7.13	7.55	4.72
Nd	25.1	23.9	28.1	20.1	27.5	24.9	26	22.9	25.8	27.1	18.2
Sm	5.02	4.22	5.46	3.98	5.37	4.91	5.06	4.62	5.45	5.29	3.37
Eu	0.983	0.967	1.11	0.88	1.11	0.995	1.05	0.981	1.01	1.07	0.821
Gd	4.26	4.02	4.8	3.68	4.64	4.39	4.57	4.18	4.6	4.65	3.13
Tb	0.686	0.651	0.753	0.59	0.746	0.676	0.712	0.651	0.732	0.725	0.501
Dy	3.83	3.52	3.99	2.84	4.17	3.75	3.84	3.66	3.95	3.9	2.92
Ho	0.76	0.742	0.821	0.54	0.828	0.756	0.778	0.736	0.829	0.796	0.52
Er	2.09	2.01	2.2	1.41	2.22	1.99	2.03	2	2.12	2.11	1.34
Tm	0.302	0.273	0.318	0.193	0.327	0.294	0.307	0.287	0.309	0.309	0.171
Yb	2.06	1.72	2.13	1.26	2.12	1.99	1.98	1.93	2.07	1.99	1.14
Lu	0.295	0.253	0.317	0.184	0.319	0.287	0.291	0.275	0.325	0.299	0.161
LREE	123	114	138	105	136	121	129	114	131	134	99
HREE	14.3	13.2	15.3	10.7	15.4	14.1	14.5	13.7	14.9	14.8	9.9
ΣREE	139	128	154	116	153	137	144	128	147	150	110
Eu/Eu*	0.933	1.03	0.952	1.01	0.976	0.941	0.963	0.98	0.887	0.944	1.11
Ce/Ce*	0.872	0.9	0.852	0.92	0.872	0.845	0.853	0.859	0.914	0.874	0.93

Section (cm)	196–197	210–211	222–223	226–227	241–242	256–257	300–301	316–317	330–331	Mean ± 1 s (*n* = 20)
La	34.3	31.4	29.2	31.7	34.2	30.9	24.9	35.1	28.3	30 ± 3.37
Ce	66.9	60.2	54.9	62.1	65.7	60.5	51.3	67.6	54.1	58.6 ± 5.64
Pr	8.18	6.41	6.93	7.62	7.92	6.94	5.12	8.35	6.81	6.94 ± 0.96
Nd	29.4	26.8	24.6	27.2	28.2	26.5	20.1	30.2	25.1	25.4 ± 3.13
Sm	5.71	4.48	4.91	5.3	5.21	5.14	3.46	5.93	4.25	4.86 ± 0.70
Eu	1.17	1.05	1	1.08	1.08	1.01	0.88	1.24	1.01	1.03 ± 0.10
Gd	4.89	4.17	4.32	4.59	4.82	4.39	3.34	5.13	3.93	4.32 ± 0.51
Tb	0.774	0.68	0.68	0.723	0.77	0.699	0.48	0.803	0.612	0.682 ± 0.085
Dy	4.23	3.78	3.77	4	4.32	3.94	2.39	4.37	3.32	3.72 ± 0.51
Ho	0.854	0.783	0.763	0.823	0.91	0.798	0.49	0.897	0.711	0.757 ± 0.115
Er	2.27	2.09	2.01	2.17	2.34	2.09	1.28	2.33	2.01	2.01 ± 0.305
Tm	0.343	0.289	0.296	0.314	0.351	0.309	0.181	0.339	0.31	0.291 ± 0.051
Yb	2.17	1.98	1.91	2.08	2.24	1.99	1.12	2.26	2.01	1.91 ± 0.34
Lu	0.332	0.271	0.285	0.307	0.361	0.298	0.171	0.346	0.291	0.283 ± 0.054
LREE	144	129	121	134	141	130	105	147	119	126 ± 14
HREE	15.9	14.0	14.0	15.0	16.1	14.5	9.5	16.5	13.2	14 ± 1.93
ΣREE	161	144	136	150	158	146	115	165	133	141 ± 15
Eu/Eu*	0.97	1.07	0.956	0.966	0.946	0.937	1.14	0.985	1.09	0.989 ± 0.065
Ce/Ce*	0.869	0.921	0.84	0.87	0.87	0.898	0.986	0.859	0.848	0.878 ± 0.049

Refer to Table 1, for water depth, latitude and longitude. Ce/Ce* denotes $Ce_{NASC}/[(La_{NASC})(Pr_{NASC})]^{1/2}$, $Eu/Eu^* = Eu_{NASC}/[(Sm_{NASC})(Gd_{NASC})]^{1/2}$. NASC = North American shale composite (Gromet et al. 1984). LREE = La + Ce + Pr + Nd + Sm; HREE = Gd + Tb + Dy + Ho + Er + Tm + Yb + Lu

6.4 Distribution of benthic foraminifera

Benthic foraminifers were analyzed throughout the two cores to look for evidence of oxygenation in sediments. Benthic foraminifers in low oxygen environments are characterized by small size and low diversity (typically 2 or 3 species make up to 80% of the population; Sen Gupta and Machain-Castillo 1993), since only a few species can adapt to such conditions and they proliferate in great numbers due to lack of competition in a food-rich environment. Therefore, its populations are very abundant (9,000–147,000 individual species per gram of sediment - Ind/g; Perez-Cruz and Machain-Castillo 1990). The foraminiferal populations identified in both cores show moderate to high diversity (number of species S = 36 (GM6)

Anaya-Gregorio *et al. Journal of Palaeogeography* (2018) 7:3

Page 15 of 19

Fig. 8 North American shale composite (NASC) normalized REE patterns for the deep-sea sediments recovered from the southwestern Gulf of Mexico (Gromet et al. 1984)
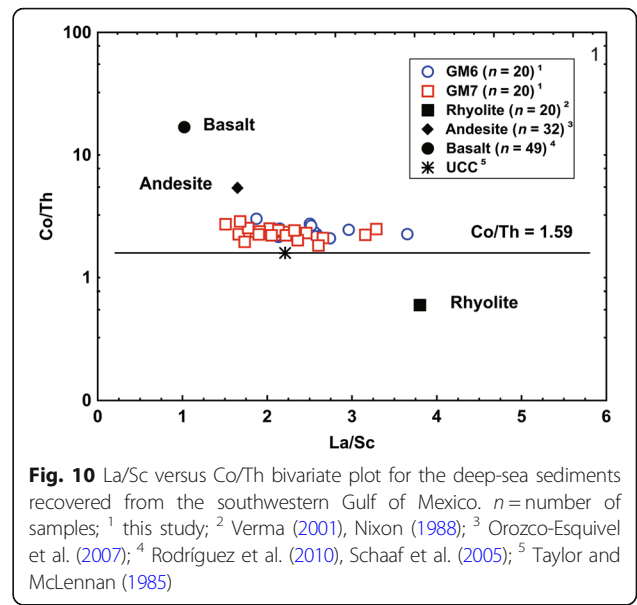

Fig. 10 La/Sc versus Co/Th bivariate plot for the deep-sea sediments recovered from the southwestern Gulf of Mexico. n = number of samples; [1] this study; [2] Verma (2001), Nixon (1988); [3] Orozco-Esquivel et al. (2007); [4] Rodríguez et al. (2010), Schaaf et al. (2005); [5] Taylor and McLennan (1985)

and S = 33 (GM7)) and abundances from 316 to 7840 Ind/g. Moreover, *Alabaminella turgida*, a species found to be sensitive to hypoxic conditions (Pflum and Frerichs 1976) is abundant throughout these cores, particularly during the Pleistocene. Another characteristic of severe hypoxia caused by enrichment of organic matter is the acidity of the water. Planktonic foraminifers dissolve easily in such environments (as the Mexican Pacific, Arellano-Torres et al. 2013) and are not well preserved or absent in the sediments beneath those environments. In the studied sediments, abundant and well preserved benthic and planktic foraminifers are found throughout the cores (Fig. 12). Similarly, our observations based on the distribution of benthic foraminifers are in agreement with the findings of Machain-Castillo et al. (1998) that

Pleistocene bathyal and abyssal waters were more oxygenated than present.

6.5 Mineralogical characterization

The low K_2O and Na_2O contents and K_2O/Na_2O ratio suggests the low proportion of K-feldspar and plagioclase in sediments (Dey et al. 2009; Nagarajan et al. 2007), which is also confirmed by XRD method in both sediment cores. The correlation between SiO_2 versus K_2O and Na_2O in the cores GM6 (r = – 0.18 and 0.39, respectively, n = 20) and GM7 (r = 0.27 and 0.19, respectively, n = 20) are low, suggesting high mobility of K and Na at the time of weathering (Armstrong-Altrin and Machain-Castillo 2016; Tawfik et al. 2017). The $K_2O/$

Fig. 9 Provenance discriminant function diagram of Roser and Korsch (1988). The discriminant functions are: Discriminant Function 1 = (– 1.773·TiO_2) + (0.607·Al_2O_3) + (0.760·Fe_2O_3) + (– 1.500·MgO) + (0.616·CaO) + (0.509·Na_2O) + (– 1.224·K_2O) + (– 9.090); Discriminant Function 2 = (0.445·TiO_2) + (0.070·Al_2O_3) + (– 0.250·Fe_2O_3) + (– 1.142·MgO) + (0.438·CaO) + (1.475·Na_2O) + (1.426·K_2O)v+ (– 6.861)
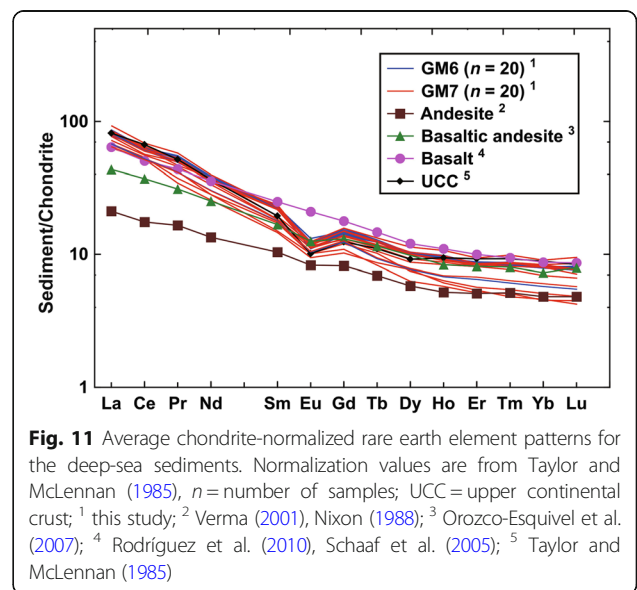

Fig. 11 Average chondrite-normalized rare earth element patterns for the deep-sea sediments. Normalization values are from Taylor and McLennan (1985), n = number of samples; UCC = upper continental crust; [1] this study; [2] Verma (2001), Nixon (1988); [3] Orozco-Esquivel et al. (2007); [4] Rodríguez et al. (2010), Schaaf et al. (2005); [5] Taylor and McLennan (1985)

Anaya-Gregorio *et al. Journal of Palaeogeography* (2018) 7:3
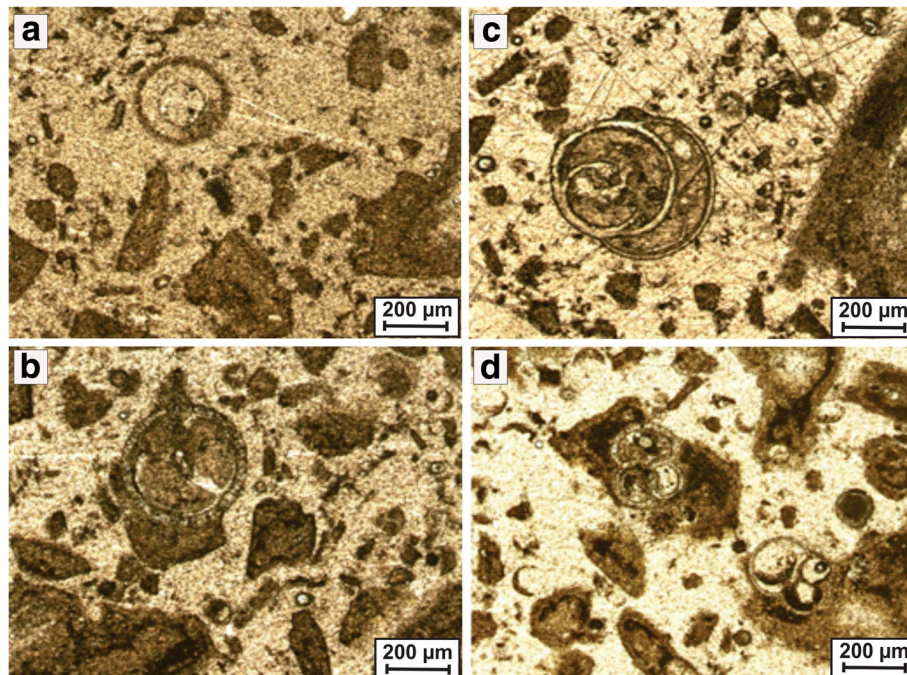
Page 16 of 19

Fig. 12 Thin-section photomicrographs taken under plane-polarized light, showing biogenic components (planktonic foraminifers, *globigerinids*). **a** GM6 (31–32 cm interval); **b** GM6 (151–152 cm interval); **c** GM7 (31–32 cm interval); **d** GM7 (151–152 cm interval)

Al_2O_3 ratio in clastic sediments may indicate the abundance of alkali feldspars and aluminosilicates, which are >5 and <5, respectively (Cox et al. 1995). The low K_2O/Al_2O_3 ratios in the GM6 (0.08–0.14) and GM7 (0.08–0.17) sediment cores indicate the higher abundance of aluminosilicates than alkali feldspars (Table 3).

The clay fraction of the GM6 and GM7 cores were dominated by kaolinite and smectite, which are related to the derivation of terrigenous materials from tropical regions (Abdullayev and Leroy 2016). Similarly, enrichment of Cr, Ga, Ni, Rb, Y, and Zn concentrations in sediments is associated to the weathering of andesite (Saha et al. 2018). The correlations between Al_2O_3 versus Nb, Y, and Zr in the cores GM6 ($r = 0.09$, $- 0.47$, and $- 0.69$, respectively, $n = 20$) and GM7 ($r = 0.26$, 0.04, and $- 0.36$, respectively, $n = 20$) are not statistically significant, suggesting that Nb, Y, and Zr are linked to the source rocks of intermediate composition and accessory detrital phases such as xenotime and zircon, respectively (Varghese et al. 2018). On the other hand, the enrichment of MnO content identified in the core sediments is most likely due to the concentration of manganosite mineral (Figs. 3c and 5). Numerous studies addressed the occurrence of manganosite in the Upper Jurassic carbonate platform shelf of the Molango Mn deposit, located near to the coastal region of the southwestern Gulf of Mexico (Johnson et al. 2016; Okita 1992; Okita and Shanks III 1992). Hence, we believe that manganosite in the core sediments was transported by the rivers to the deep-sea area of the Gulf of Mexico.

We consider that the enrichment of CaO in sediments is due to the distribution of sand-size benthic foraminifers, which is also identified at intervals of 256–257 cm (GM6) (Fig. 4a, b) and 300–301 cm (GM7) (Fig. 4c, d). In addition, the presence of calcite is related to the ability of smectite to observe cations such as Ca^{2+} to the surface of its crystalline structure (Abdullayev and Leroy 2016). Sulfate content identified in both cores by SEM-EDS represents the pyrite mineral (Fig. 4e, f). According to Berner (1984), pyrite is a widespread mineral and most marine sediments contain at least traces of it, since it forms during shallow burial by the reaction of detrital iron minerals with H_2S produced by bacterial sulfate reduction. The environment where this occurs is few centimeters below the water-surface interface. Most foraminifers live at the sediment water interface or just below it. Therefore, the foraminifers in the studied sediments were living under oxic conditions as revealed by their abundance, diversity and degree of preservation. Berner (1984) further indicated that in anoxic marine sediments, the high supply of organic matter and H_2S produce high concentrations of pyrite, which is not the case of the sediments studied, as seen in Figs. 3 and 4.

7 Conclusions

The compositional variations of two sediment cores recovered at the southwestern Gulf of Mexico were analyzed to infer their age and provenance. Texturally, the

Anaya-Gregorio et al. Journal of Palaeogeography (2018) 7:3

Page 17 of 19

sediments are classified as silt and clay, and chemically as shale, indicating the domination of fine-grained sediments in both cores. Based on the radiocarbon ages the Pleistocene/Holocene boundary is identified at 130 cm interval. The weathering indices (CIA, CIW, and PIA) indicated a moderate to high intensity of weathering.

The concentrations of major element, transition trace elements, and the similarity between the chondrite- normalized REE patterns of the deep-sea sediments and the source rocks revealed that the depositional basin received sediments from the intermediate igneous rocks like andesite and basaltic andesite, at least during the last 23,615 cal yrs. BP.

The enrichment of Zn content in two intervals reveals an influence of anthropogenic input such as pesticides and agricultural waste in modern times. The authigenic uranium content, Ce anomaly, V/Cr and Ni/Co ratios and the distribution of benthic foraminifers suggested that the sediments were deposited in an oxic depositional condition. The similarity in geochemical composition between the two sediment cores reveals that the depositional condition in the deep-sea area of the southwestern Gulf of Mexico was similar at least in the last 23,615 cal yrs.

Publisher's Note
Springer Nature remains neutral with regard to jurisdictional claims in published maps and institutional affiliations.

Author details
[1]Licenciatura en Ingeniería en Geología Ambiental, Área Académica de Ciencias de la Tierra y Materiales, Universidad Autónoma del Estado de Hidalgo, Mineral de la Reforma, Hidalgo, Mexico. [2]Instituto de Ciencias del Mar y Limnología, Universidad Nacional Autónoma de México, Unidad de Procesos Oceánicos y Costeros, Ciudad Universitaria, 04510 Ciudad de México, Mexico. [3]Área Académica de Ciencias de la Tierra y Materiales, Universidad Autónoma del Estado de Hidalgo, Ciudad Universitaria, Carretera Pachuca-Tulancingo Km 4.5, Col. Carboneras, C.P. 42184 Mineral de la Reforma, Hidalgo, Mexico. [4]Posgrado en Ciencias del Mar y Limnología, Universidad Nacional Autónoma de México, Ciudad Universitaria, 3000, Coyoacán, C.P. 04510 Ciudad de México, Mexico.

References
Abdullayev, E., and S.A.G. Leroy. 2016. Provenance of clay minerals in the sediments from the Pliocene productive series, western South Caspian Basin. *Marine and Petroleum Geology* 73: 517–527.

Arellano-Torres, E., M.L. Machain-Castillo, L.A. Contreras-Rosales, L.B. Cuesta-Castillo, and A.C. Ruiz-Fernández. 2013. Foraminiferal faunal evidence for glacial–interglacial variations in the ocean circulation and the upwelling of the Gulf of Tehuantepec (Mexico). *Marine Micropaleontology* 100: 52–66.

Armstrong-Altrin, J.S. 2009. Provenance of sands from Cazones, Acapulco, and Bahía Kino beaches, México. *Revista Mexicana de Ciencias Geológicas* 26 (3): 764–782.

Armstrong-Altrin, J.S. 2015. Evaluation of two multidimensional discrimination diagrams from beach and deep-sea sediments from the Gulf of Mexico and their application to Precambrian clastic sedimentary rocks. *International Geology Review* 57 (11–12): 1446–1461.

Armstrong-Altrin, J.S., Y.I. Lee, J.J. Kasper-Zubillaga, A. Carranza-Edwards, D. Garcia, G.N. Eby, V. Balaram, and N.L. Cruz-Ortiz. 2012. Geochemistry of beach sands along the western Gulf of Mexico, Mexico: Implication for provenance. *Chemie der Erde - Geochemistry* 72 (4): 345–362.

Armstrong-Altrin, J.S., Y.I. Lee, J.J. Kasper-Zubillaga, and E. Trejo-Ramírez. 2017. Mineralogy and geochemistry of sands along the Manzanillo and El Carrizal beach areas, southern Mexico: Implications for palaeoweathering, provenance and tectonic setting. *Geological Journal* 52 (4): 559–582.

Armstrong-Altrin, J.S., and M.L. Machain-Castillo. 2016. Mineralogy, geochemistry, and radiocarbon ages of deep sea sediments from the Gulf of Mexico, Mexico. *Journal of South American Earth Sciences* 71: 182–200.

Armstrong-Altrin, J.S., M.L. Machain-Castillo, L. Rosales-Hoz, A. Carranza-Edwards, J. Sanchez-Cabeza, and A.C. Ruíz-Fernández. 2015a. Provenance and depositional history of continental slope sediments in the southwestern Gulf of Mexico unraveled by geochemical analysis. *Continental Shelf Research* 95: 15–26.

Armstrong-Altrin, J.S., R. Nagarajan, V. Balaram, and O. Natalhy-Pineda. 2015b. Petrography and geochemistry of sands from the Chachalacas and Veracruz beach areas, western Gulf of Mexico, Mexico: Constraints on provenance and tectonic setting. *Journal of South American Earth Sciences* 64 (Part 1): 199–216.

Armstrong-Altrin, J.S., R. Nagarajan, Y.I. Lee, J.J. Kasper-Zubillaga, and L.P. Córdoba-Saldaña. 2014. Geochemistry of sands along the San Nicolás and San Carlos beaches, Gulf of California, Mexico: Implication for provenance. *Turkish Journal of Earth Sciences* 23 (5): 533–558.

Basu, A. 2017. Evolution of siliciclastic provenance inquiries: A critical appraisal. In *Sediment provenance. Chapter 2*, ed. R. Mazumder, 5–23. Netherlands: Elsevier Amsterdam. https://doi.org/10.1016/B978-0-12-803386-9.00002-2.

Berner, R.A. 1984. Sedimentary pyrite formation: An update. *Geochimica et Cosmochimica Acta* 48 (4): 605–615.

Bhattacharjee, J., K.K. Ghosh, and B. Bhattacharya. 2017. Petrography and geochemistry of sandstone–mudstone from Barakar formation (early Permian), Raniganj Basin, India: Implications for provenance, weathering and marine depositional conditions during lower Gondwana sedimentation. *Geological Journal*. https://doi.org/10.1002/gj.2946. in press.

Carranza-Edwards, A., E. Centeno-Garcia, L. Rosales-Hoz, and R. Lozano Santacruz. 2001. Provenance of beach gray sands from western México. *Journal of South American Earth Sciences* 14 (3): 291–305.

Cox, R., D.R. Lowe, and R.L. Cullers. 1995. The influence of sediment recycling and basement composition on evolution of mudrock chemistry in the southwestern United States. *Geochimica et Cosmochimica Acta* 59 (14): 2919–2940.

Anaya-Gregorio *et al. Journal of Palaeogeography* (2018) 7:3

Page 18 of 19

Craigie, N. 2018. Production of chemostratigraphic correlation schemes. In *Principles of elemental Chemostratigraphy. Advances in oil and gas exploration and production*, 85–129. Cham: Springer.

Cullers, R.L., B. Bock, and C. Guidotti. 1997. Elemental distributions and neodymium isotopic compositions of Silurian metasediments, western Maine, USA: Redistribution of the rare earth elements. *Geochimica et Cosmochimica Acta* 61 (9): 1847–1861.

Day, J.W., A. Yañéz-Arancibia, W.J. Mitsch, A.L. Lara-Dominguez, J.N. Day, J.-Y. Ko, R. Lane, J. Lindsey, and D.Z. Lomeli. 2003. Using ecotechnology to address water quality and wetland habitat loss problems in the Mississippi Basin: A hierarchical approach. *Biotechnology Advances* 22 (1): 135–159.

Dey, S., A.K. Rai, and A. Chaki. 2009. Palaeoweathering, composition and tectonics of provenance of the Proterozoic intracratonic Kaladgi–Badami Basin, Karnataka, southern India: Evidence from sandstone petrography and geochemistry. *Journal of Asian Earth Sciences* 34 (6): 703–715.

Elderfield, H., and M.J. Greaves. 1982. The rare earth elements in seawater. *Nature* 296 (5854): 214–219.

Fedo, C.M., H.W. Nesbitt, and G.M. Young. 1995. Unraveling the effects of potassium metasomatism in sedimentary-rocks and paleosols, with implications for paleoweathering conditions and provenance. *Geology* 23 (10): 921–924.

Feng, R., and R. Kerrich. 1992. Geochemical evolution of granitoids from the Archean Abitibi southern volcanic zone and the Pontiac subprovince, Superior Province, Canada: Implications for tectonic history and source regions. *Chemical Geology* 98 (1–2): 23–70.

Folk, R.L. 1980. *Petrology of sedimentary rocks*, 182. Austin: Hemphill Publishing Company.

Goldberg, K., and M. Humayun. 2016. Geochemical paleoredox indicators in organic-rich shales of the Irati formation, Permian of the Paraná Basin, southern Brazil. *Brazilian Journal of Geology* 46 (3): 377–393.

Gromet, L.P., L.A. Haskin, R.L. Korotev, and R.F. Dymek. 1984. The "north American shale composite": Its compilation, major and trace element characteristics. *Geochimica et Cosmochimica Acta* 48 (12): 2469–2482.

Harnois, L. 1988. The CIW index: A new chemical index of weathering. *Sedimentary Geology* 55 (3–4): 319–322.

Hernández-Hinojosa, V., P.C. Montiel-García, J.S. Armstrong-Altrin, R. Nagarajan, and J.J. Kasper-Zubillaga. 2018. Textural and geochemical characteristics of beach sands along the western Gulf of Mexico, Mexico. *Carpathian Journal of Earth and Environmental Sciences* 13 (1): 161–174.

Herron, M.M. 1988. Geochemical classification of terrigenous sands and shales from core or log data. *Journal of Sedimentary Research* 58 (5): 820–829.

Hou, Q., C.L. Mou, Q.Y. Wang, and Z.Y. Tan. 2017. Provenance and tectonic setting of the early and middle Devonian Xueshan formation, the north Qilian Belt, China. *Geological Journal*. https://doi.org/10.1002/gj.2963. in press.

Jarvis, K.E. 1988. Inductively coupled plasma mass spectrometry: A new technique for the rapid or ultra-trace level determination of the rare-earth elements in geological materials. *Chemical Geology* 68 (1): 31–39.

Johnson, J.E., S.M. Webb, C. Ma, and W.W. Fischer. 2016. Manganese mineralogy and diagenesis in the sedimentary rock record. *Geochimica et Cosmochimica Acta* 173: 210–231.

Jones, B., and D.A.C. Manning. 1994. Comparison of geochemical indices used for the interpretation of palaeoredox conditions in ancient mudstones. *Chemical Geology* 111: 111–129.

Kasper-Zubillaga, J.J., J.S. Armstrong-Altrin, A. Carranza-Edwards, O. Morton-Bermea, and R. Lozano Santacruz. 2013. Control in beach and dune sands of the Gulf of Mexico and the role of nearby rivers. *International Journal of Geosciences* 4 (8): 1157–1174.

Kennett, J.P., K. Elmstrom, and N. Penrose. 1985. The last deglaciation in Orca Basin, Gulf of Mexico: High-resolution planktonic foraminiferal changes. *Palaeogeography, Palaeoclimatology, Palaeoecology* 50 (2–3): 189–216.

Kennett, J.P., and P. Huddlestun. 1972. Late Pleistocene paleoclimatology, foraminiferal biostratigraphy and tephrochronology, western Gulf of Mexico. *Quaternary Research* 2 (1): 38–69.

Lozano, R., and J.P. Bernal. 2005. Characterization of a new set of eight geochemical reference materials for XRF major and trace element analysis. *Revista Mexicana de Ciencias Geológicas* 22: 329–344.

Machain-Castillo, M.-L., B.K. Sen Gupta, and J.A. Alcala Herrera. 1998. Late quaternary change in deep-bathyal and abyssal waters of the Gulf of Mexico: Preservation record of the foraminifer *Biloculinella irregularis*. *Journal of Foraminiferal Research* 28 (2): 95–101.

Madhavaraju, J., S.A. Pacheco-Olivas, C.M. González-León, I.G. Espinoza-Maldonado, P.A. Sanchez-Medrano, U. Villanueva-Amadoz, R. Monreal, T. Pi-Puig, E. Ramírez-Montoya, and F.J. Grijalva-Noriega. 2017. Mineralogy and geochemistry of the lower cretaceous siliciclastic rocks of the Morita formation, sierra San José section, Sonora, Mexico. *Journal of South American Earth Sciences* 76: 397–411.

Madhavaraju, J., M. Tom, Y.I. Lee, V. Balaram, S. Ramasamy, A. Carranza-Edwards, and A. Ramachandran. 2016. Provenance and tectonic settings of sands from Puerto Peñasco, Desemboque and Bahia Kino beaches, gulf of California, Sonora, México. *Journal of South American Earth Sciences* 71: 262–275.

Mitra, R., G. Chakrabarti, and D. Shome. 2017. Geochemistry of the Palaeo–Mesoproterozoic Tadpatri shales, Cuddapah Basin, India: Implications on provenance, paleoweathering and paleoredox conditions. *Acta Geochimica*. https://doi.org/10.1007/s11631-017-0254-3. in press.

Nagarajan, R., J.S. Armstrong-Altrin, F.L. Kessler, and J. Jong. 2017. Petrological and geochemical constraints on provenance, paleo-weathering and tectonic setting of clastic sediments from the Neogene Lambir and Sibuti Formations, northwest Borneo. In *Sediment provenance. Chapter 7*, ed. R. Mazumder, 123–153. Netherlands: Elsevier Amsterdam.

Nagarajan, R., J. Madhavaraju, R. Nagendra, J.S. Armstrong-Altrin, and J. Moutte. 2007. Geochemistry of Neoproterozoic shales of the Rabanpalli formation, Bhima Basin, northern Karnataka, southern India: Implications for provenance and paleoredox conditions. *Revista Mexicana de Ciencias Geológicas* 24 (2): 150–160.

Nesbitt, H.W., and G.M. Young. 1982. Early Proterozoic climates and plate motions inferred from major element chemistry of lutites. *Nature* 299 (5885): 715–717.

Nixon, G.T. 1988. Petrology of the younger andesites and dacites of Iztaccíhuatl volcano, Mexico: II. Chemical stratigraphy, magma mixing, and the composition of basaltic magma influx. *Journal of Petrology* 29 (2): 265–303.

Okita, P.M. 1992. Manganese carbonate mineralization in the Molango District, Mexico. *Economic Geology* 87 (5): 1345–1366.

Okita, P.M., and W.C. Shanks III. 1992. Origin of stratiform sediment-hosted manganese carbonate ore deposits: Examples from Molango, Mexico, and TaoJiang, China. *Chemical Geology* 99 (1–3): 139–163.

Orozco-Esquivel, T., C.M. Petrone, L. Ferrari, T. Tagami, and P. Manetti. 2007. Geochemical and isotopic variability in lavas from the eastern trans-Mexican Volcanic Belt: Slab detachment in a subduction zone with varying dip. *Lithos* 93 (1–2): 149–174.

Paikaray, S., S. Banerjee, and S. Mukherji. 2008. Geochemistry of shales from the Paleoproterozoic to Neoproterozoic Vindhyan Supergroup: Implications on provenance, tectonics and paleoweathering. *Journal of Asian Earth Sciences* 32 (1): 34–48.

Papadopoulos, A., A. Koroneos, G. Christofides, L. Papadopoulou, I. Tzifas, and S. Stoulos. 2016. Assessment of gamma radiation exposure of beach sands in highly touristic areas associated with plutonic rocks of the Atticocycladic zone (Greece). *Journal of Environmental Radioactivity* 162–163: 235–243.

Perez-Cruz, L.L., and M.L. Machain-Castillo. 1990. Benthic foraminifera of the oxygen minimum zone, continental shelf of the Gulf of Tehuantepec, Mexico. *Journal of Foraminiferal Research* 20 (4): 312–325.

Periasamy, V., and M. Venkateshwarlu. 2017. Petrography and geochemistry of Jurassic sandstones from the Jhuran formation of Jara dome, Kachchh Basin, India: Implications for provenance and tectonic setting. *Journal of Earth System Science* 126 (4): 44.

Pflum, C.E., and W.E. Frerichs. 1976. Gulf of Mexico deep-water foraminifers. *Cushman Foundation for Foraminiferal Research Special Publication* 14: 1–125.

Ramos-Vázquez, M.A., J.S. Armstrong-Altrin, L. Rosales-Hoz, M.L. Machain-Castillo, and A. Carranza-Edwards. 2017. Geochemistry of deep-sea sediments in two cores retrieved at the mouth of the Coatzacoalcos River delta, western Gulf of Mexico, Mexico. *Arabian Journal of Geosciences* 10 (6): 148.

Rodríguez, S.R., W. Morales-Barrera, P. Layer, and E. González-Mercado. 2010. A quaternary monogenetic volcanic field in the Xalapa region, eastern trans-Mexican Volcanic Belt: Geology, distribution and morphology of the volcanic vents. *Journal of Volcanology and Geothermal Research* 197 (1): 149–166.

Rosales-Hoz, L., A. Carranza-Edwards, R.G. Martínez-Serrano, M.A. Alatorre, and J.S. Armstrong-Altrin. 2015. Textural and geochemical characteristics of marine sediments in the SW Gulf of Mexico: Implications for source and seasonal change. *Environmental Monitoring Assessment* 187 (4): 205.

Roser, B.P., and R.J. Korsch. 1988. Provenance signatures of sandstone–mudstone suites determined using discriminant function analysis of major-element data. *Chemical Geology* 67 (1–2): 119–139.

Saha, S., S. Banerjee, S.D. Burley, A. Ghosh, and P.K. Saraswati. 2010. The influence of flood basaltic source terrains on the efficiency of tectonic setting discrimination diagrams: An example from the Gulf of Khambhat, western India. *Sedimentary Geology* 228 (1–2): 1–13.

Anaya-Gregorio *et al. Journal of Palaeogeography* (2018) 7:3

Page 19 of 19

Saha, S., S. Burley, and S. Banerjee. 2018. Mixing processes in modern estuarine sediments from the Gulf of Khambhat, western India. *Marine and Petroleum Geology* 91: 599–621.

Salas-de-León, D.A., M.A. Monreal-Gómez, M.A. Díaz-Flores, D. Salas-Monreal, H. Velasco-Mendoza, M.L. Riverón-Enzástiga, and G. Ortiz-Zamora. 2008. Role of near-bottom currents in the distribution of sediments within the Southern Bay of Campeche, Gulf of Mexico. *Journal of Coastal Research* 24 (6): 1487–1494.

Schaaf, P., J. Stimac, C. Siebe, and J.L. Macías. 2005. Geochemical evidence for mantle origin and crustal processes in volcanic rocks from Popocatépetl and surrounding monogenetic volcanoes, Central Mexico. *Journal of Petrology* 46 (6): 1243–1282.

Selvaraj, K., T.Y. Lee, J.Y.T. Yang, E.A. Canuel, J.C. Huang, M. Dai, J.T. Liu, and S.J. Kao. 2015. Stable isotopic and biomarker evidence of terrigenous organic matter export to the deep sea during tropical storms. *Marine Geology* 364: 32–42.

Sen Gupta, B.K., and M.L. Machain-Castillo. 1993. Benthic foraminifera in oxygen-poor habitats. *Marine Micropaleontology* 20 (3–4): 183–201.

Solari, L.A., R. Torres de León, G. Hernández Pineda, J. Solé, G. Solís-Pichardo, and T. Henández-Treviño. 2007. Tectonic significance of cretaceous–tertiary magmatic and structural evolution of the northern margin of the Xolapa complex, Tierra Colorada area, southern Mexico. *GSA Bulletin* 119 (9): 1265–1279.

Stuiver, M., and P.J. Reimer. 1993. Extended ^{14}C database and revised CALIB radiocarbon calibration program. *Radiocarbon* 35 (1): 215–230.

Tapia-Fernandez, H.J., J.S. Armstrong-Altrin, and K. Selvaraj. 2017. Geochemistry and U–Pb geochronology of detrital zircons in the Brujas beach sands, Campeche, southwestern Gulf of Mexico, Mexico. *Journal of South American Earth Sciences* 76: 346–361.

Tawfik, H.A., M.K. Salah, W. Maejima, J.S. Armstrong-Altrin, A.-M.T. Abdel-Hameed, M.M. El Ghandour, and A. Ruffell. 2017. Petrography and geochemistry of the lower Miocene Moghra sandstones, Qattara depression, north Western Desert, Egypt. *Geological Journal*. https://doi.org/10.1002/gj.3025. in press.

Taylor, S.R., and S.M. McLennan. 1985. *The continental crust: Its composition and evolution*. London: Blackwell Scientific Publications.

Tostevin, R., G.A. Shields, G.M. Tarbuck, T. He, M.O. Clarkson, and R.A. Wood. 2016. Effective use of cerium anomalies as a redox proxy in carbonate-dominated marine settings. *Chemical Geology* 438: 146–162.

Tzifas, I.T., P. Misaelides, A. Godelitsas, P.N. Gamaletsos, P. Nomikou, A.G. Karydas, V. Kantarelou, and A. Papadopoulos. 2017. Geochemistry of coastal sands of eastern Mediterranean: The case of Nisyros volcanic materials. *Chemie der Erde - Geochemistry* 77: 487–501.

Varghese, T.I., P.T. Nageshrao, N. Raghavendramurthy, and N. Ramasamy. 2018. Sediment geochemistry of coastal environments, southern Kerala, India: Implication for provenance. *Arabian Journal of Geosciences* 11 (3): 61.

Verma, S.P. 2001. Geochemical evidence for a rift-related origin of bimodal volcanism at Meseta Rio San Juan, north-central Mexican volcanic belt. *International Geology Review* 43 (6): 475–493.

Verma, S.P., and J.S. Armstrong-Altrin. 2016. Geochemical discrimination of siliciclastic sediments from active and passive margin settings. *Sedimentary Geology* 332 (1): 1–12.

Verma, S.P., L. Díaz-González, and J.S. Armstrong-Altrin. 2016a. Application of a new computer program for tectonic discrimination of Cambrian to Holocene clastic sediments. *Earth Science Informatics* 9 (2): 151–165.

Verma, S.P., D. Torres-Sánchez, F. Velasco-Tapia, K.S.V. Subramanyam, C. Manikyamba, and R. Bhutani. 2016b. Geochemistry and petrogenesis of extension-related magmas close to the volcanic front of the central part of the trans-Mexican Volcanic Belt. *Journal of South American Earth Sciences* 72: 126–136.

Wang, Z.W., X.G. Fu, X.L. Feng, C.Y. Song, D. Wang, W.B. Chen, and S.Q. Zeng. 2017a. Geochemical features of the black shales from the Wuyu Basin, southern Tibet: Implications for palaeoenvironment and palaeoclimate. *Geological Journal* 52 (2): 282–297.

Wang, Z.W., J. Wang, X.G. Fu, X.L. Feng, D. Wang, C.Y. Song, W.B. Chen, and S.Q. Zeng. 2017c. Petrography and geochemistry of upper Triassic sandstones from the Tumengela formation in the Woruo Mountain area, north Qiangtang Basin, Tibet: Implications for provenance, source area weathering, and tectonic setting. *Island Arc* 26 (4): e12191.

Wang, Z.W., J. Wang, X.G. Fu, X.L. Feng, D. Wang, C.Y. Song, W.B. Chen, S.Q. Zeng, and F. Yu. 2017d. Provenance and tectonic setting of the Quemoco sandstones in the north Qiangtang Basin, North Tibet: Evidence from geochemistry and detrital zircon geochronology. *Geological Journal*. https://doi.org/10.1002/gj.2967. in press.

Wang, Z.W., J. Wang, X.G. Fu, W.Z. Zhan, F. Yu, X.L. Feng, C.Y. Song, W.B. Chen, and S.Q. Zeng. 2017b. Organic material accumulation of Carnian mudstones in the north Qiangtang depression, eastern Tethys: Controlled by the paleoclimate, paleoenvironment, and provenance. *Marine and Petroleum Geology* 88: 440–457.

Wignall, P.B., and K.J. Myers. 1988. Interpreting benthic oxygen levels in mudrocks: A new approach. *Geology* 16 (5): 452–455.

Zaid, S.M. 2013. Provenance, diagenesis, tectonic setting and reservoir quality of the sandstones of the Kareem Formation, Gulf of Suez, Egypt. *Journal of African Earth Sciences* 85: 31–52.

Zaid, S.M. 2015. Geochemistry of sandstones from the Pliocene Gabir formation, north Marsa Alam, Red Sea, Egypt: Implication for provenance, weathering and tectonic setting. *Journal of African Earth Sciences* 102: 1–17.

Zaid, S.M., O. El-Badry, and A.M. Abdel-Fatah. 2017. Provenance of pharaonic potsherds, Sharkiya governorate, Egypt. *Arabian Journal of Geosciences* 10 (16): 354.

Zaid, S.M., O. El-Badry, F. Ramadan, and M. Mohamed. 2015. Petrography and geochemistry of pharaonic sandstone monuments in tall san Al Hagr, Al Sharqiya governorate, Egypt: Implications for provenance and tectonic setting. *Turkish Journal of Earth Sciences* 24 (4): 344–364.